
A NOVEL MESH REGULARIZATION APPROACH BASED ON FINITE ELEMENT DISTORTION POTENTIALS: APPLICATION TO MATERIAL EXPANSION PROCESSES WITH EXTREME VOLUME CHANGE

Abhiroop Satheesh, Christoph P. Schmidt, Wolfgang A. Wall, Christoph Meier

Institute for Computational Mechanics
Technical University of Munich
Garching, Germany, 85748

ABSTRACT

The accuracy of finite element solutions is closely tied to the mesh quality. In particular, geometrically nonlinear problems involving large and strongly localized deformations often result in prohibitively large element distortions. In this work, we propose a novel mesh regularization approach allowing to restore a non-distorted high-quality mesh in an adaptive manner without the need for expensive re-meshing procedures. The core idea of this approach lies in the definition of a finite element distortion potential considering contributions from different distortion modes such as skewness and aspect ratio of the elements. The regularized mesh is found by minimization of this potential. Moreover, based on the concept of spatial localization functions, the method allows to specify tailored requirements on mesh resolution and quality for regions with strongly localized mechanical deformation and mesh distortion. In addition, while existing mesh regularization schemes often keep the boundary nodes of the discretization fixed, we propose a mesh-sliding algorithm based on variationally consistent mortar methods allowing for an unrestricted tangential motion of nodes along the problem boundary. Especially for problems involving significant surface deformation (e.g., frictional contact), this approach allows for an improved mesh relaxation as compared to schemes with fixed boundary nodes. To transfer data such as tensor-valued history variables of the material model from the old (distorted) to the new (regularized) mesh, a structure-preserving invariant interpolation scheme for second-order tensors is employed, which has been proposed in our previous work and is designed to preserve important mechanical properties of tensor-valued data such as objectivity and positive definiteness. As a practically relevant application scenario, we consider the thermo-mechanical expansion of materials such as foams involving extreme volume changes by up to two orders of magnitude along with large strains as well as thermo-mechanical contact interaction. For this scenario it is demonstrated that the proposed regularization approach preserves a high mesh quality at small computational costs. In contrast, simulations without mesh adaption are shown to lead to significant mesh distortions and, eventually, to large discretization errors or even non-convergence of the numerical solution scheme.

1 Introduction

The accuracy of finite element solutions is closely tied to the quality of the underlying finite element mesh. Moreover, element distortion can result in unreliable solutions or even lead to divergence. Therefore, it is important to keep mesh distortions small to achieve accurate and reliable results. To address this issue, dynamic mesh treatment techniques such as h - and r -refinement have been developed and studied. In general, replacing the old mesh by a newly generated mesh (h -refinement) is typically a computationally inefficient approach as it results in high CPU costs and challenges regarding parallel communication. Furthermore, it requires additional means for maintaining mesh quality. In contrast, mesh adaptation, which allows for updating the mesh without consuming excessive computational resources, seems to be a more efficient and flexible approach. Mesh adaptation typically consists of two major steps viz. finding the new nodal positions (new mesh) and transferring the data from old to new mesh. In this work, to avoid ambiguities, we term

the first step as *mesh refitting* and the second step as *data transfer*, while the overall procedure including both steps is termed *mesh adaptation*.

Mesh refitting techniques have been studied in the past, e.g., in the context of fluid-structure interaction based on arbitrary Lagrangian-Eulerian (ALE) discretizations. These methods can be classified as interpolation and physical analogy-based methods. A detailed review of mesh refitting methods can be found in [1]. In interpolation-based schemes, an interpolation function is used to obtain the new mesh and in general they do not require nodal connectivity information, which enables their application to polyhedral elements or unstructured grids. The most common methods in this category are transfinite interpolation [2], the algebraic damping method [3], and radial basis function interpolation [4]. Transfinite interpolation has the disadvantage of producing inverted elements, while the algebraic damping method may yield non-smooth aspect ratio distributions in the domain. Additionally, the use of radial basis function methods can be computationally expensive. In contrast, physical analogy-based methods use the element connectivity information and find the new nodal location by solving a system of equations formulated according to a physical process. The first in this class is the linear spring analogy approach proposed by Batina [5]. In this method, a fictitious spring is added to the discretization with a stiffness inversely proportional to the element edge length. This method frequently results in inverted elements and is less suited for large deformation problems. To prevent element inversion, modified spring analogies such as torsional spring [6], semi-torsional spring [7], ball-vertex [8], and ortho-semi-torsional spring approaches were proposed. However, these methods are either limited to triangular (tetrahedral in 3D) elements or have been shown to exhibit poor performance for large deformation problems. Moreover, these methods can also result in inverted elements or boundary nodes that are not relaxed. Another set of methods in this group is given by Laplacian methods [9, 10], in which a Laplace equation is solved in the interior of the domain. These schemes allow for a certain degree of regularization for distorted meshes and they ensure that the interior nodes remain confined by the domain boundaries. However, Laplacian methods often result in a limited mesh movement and may also lead to inverted elements (see [10]). Finally, in an elastostatic approach [11, 12], the discretized domain is considered as an elastic body and the new nodal locations are obtained through the solution of an elasticity problem. Here, the new nodal locations are dependent on the Young's modulus and the Poisson's ratio of the pseudo-elastic problem. Yet, a linear elastostatic equation can lead to inverted elements and non-linear constitutive equations can lead to poor element quality for large deformation problems. Improved elastostatic approaches can be found in [13, 14, 15]. Still, these methods suffer from insufficient element quality control and are not well-suited for large deformation problems with localized large mesh distortion.

In summary, there is still a need for refitting techniques that can produce a high quality mesh for problems involving very large deformation, especially if this deformation is strongly localized. Existing methods tend to give either inverted elements or elements with low quality in such scenarios. Moreover, controlling the element size at specific regions of the domain is not easily feasible with existing approaches. In addition, the mesh movement for boundary nodes is either limited or for some approaches even impossible, leading to distorted elements at the boundary. To overcome these issues, we propose a novel mesh refitting technique based on the definition of an element distortion potential together with mortar schemes for mesh sliding at the domain boundaries. The mortar mesh sliding schemes facilitate the movement of boundary elements and thereby help to achieve a high quality mesh at the boundary. We demonstrate the effectiveness of the proposed mesh refitting technique by means of several numerical examples. It is demonstrated that the method is well-suited for problems involving large volume expansion, even for the challenging case of strongly localized deformations and mesh distortions.

Once the new mesh is obtained, the primary and history variables must be mapped from old to new discretization. The accuracy of the data mapping between the meshes is critical for all adaptive FEM procedures. The most common data types that arise as history variables are scalars and tensors. On the one hand, the mapping of scalar variables is well investigated, and methods such as moving least squares can be adopted [16, 17, 18, 19, 20, 21]. On the other hand, the mapping of tensor-valued data was not well-studied before [22]. To bridge this gap, structure preserving tensor interpolation schemes have been proposed and evaluated in the author's previous work [22]. These interpolation schemes fulfill essential properties of the underlying continuum mechanics problem such as objectivity, positive definiteness, and monotonicity of invariants of the interpolated tensors along with higher-order spatial convergence.

In the present work, we propose a novel mesh adaptation scheme. The method is based on the definition of an element distortion potential considering contributions from different distortion modes such as skewness and aspect ratio of the elements. The regularized mesh is obtained by minimizing this potential. Furthermore, we use spatial functions to achieve mesh localization, i.e., specified mesh quality at selected regions of the domain. Such a function helps to satisfy tailored mesh resolution and quality requirements for problems with strongly localized mechanical deformation and mesh distortion. To address also problems involving significant surface deformation, we employ a mortar mesh-sliding scheme to allow for a tangential movement of boundary nodes without changing the boundary topology. It is demonstrated that this approach enables a significantly improved mesh relaxation as compared to schemes with fixed boundary nodes. To transfer tensor-valued history data from the old to the new mesh, we utilize the structure-preserving

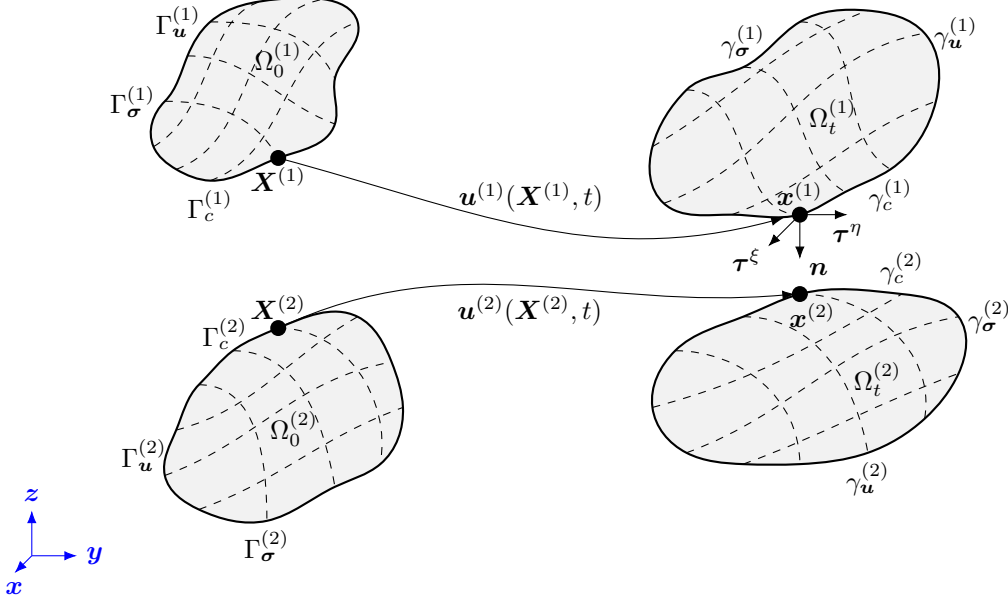


Figure 1: Notation and kinematics to depict the interaction between two deformable bodies.

interpolation methods proposed in our previous work [22]. Based on selected numerical examples involving materials with a large volume expansion by up to two orders of magnitude, we demonstrate that the proposed approach is well-suited for large deformation problems, particularly for strongly localized distortions, while the resulting additional computational costs are small compared to simulations without mesh adaption.

The paper is organized as follows: first, the underlying thermo-mechanical problem is presented in Section 2. In the problem definition, the finite inelastic material model is introduced in Section 2.2, followed by mortar thermo-mechanical contact in Section 2.3, and finally the space and time discretization Section 2.4. Next, the mesh adaptation method is detailed in Section 3 in which the mesh refitting problem is formulated in Section 3.1, and the data transfer methods are described in Section 3.2. Then the numerical results are presented in Section 4. Lastly, the summary and concluding remarks are given in Section 5.

2 Thermo-mechanical problem

In this work, we propose a novel mesh adaption method, which is able to regularize strongly distorted meshes without the need for a complete remeshing. The proposed method is applied to a finite deformation thermo-mechanical problem involving thermally activated materials undergoing very large (inelastic) volume expansion as well as thermo-mechanical contact interaction, which typically results in prohibitively large mesh distortions if no mesh adaption is applied. We start with a description of the underlying thermo-mechanical problem. Next, the thermo-mechanical constitutive model for the inelastic expansion is presented, followed by the thermo-mechanical contact formulation.

2.1 Thermo-mechanical initial boundary value problem

Consider the deformation of bodies $i = \{1, 2\}$ with reference configuration $\mathbf{X}^{(i)} \in \Omega_0^{(i)}$ and current configuration $\mathbf{x}^{(i)} \in \Omega_t^{(i)}$ at time t described by the mapping $\varphi_t^{(i)} : \mathbf{X}^{(i)} \mapsto \mathbf{x}^{(i)}$ as illustrated in Figure 1. The displacement $\mathbf{u}^{(i)}$ at material point $\mathbf{X}^{(i)}$ is given by $\mathbf{u}^{(i)}(\mathbf{X}^{(i)}, t) = \mathbf{x}^{(i)}(t) - \mathbf{X}^{(i)}$ and the temperature is denoted by $T^{(i)}(\mathbf{X}^{(i)}, t)$. The thermo-mechanical initial boundary value problem (IBVP) summarizing the set of equations required to determine the

displacement and temperature evolution, i.e. the primary variables $\mathbf{u}^{(i)}$ and $T^{(i)}$ in the time interval $t \in [0, t^E]$, reads:

$$\begin{aligned}
\nabla_{\mathbf{X}} \cdot (\mathbf{F}^{(i)} \mathbf{S}^{(i)}) + \hat{\mathbf{b}}_0^{(i)} &= \rho_0^{(i)} \ddot{\mathbf{u}}^{(i)} && \text{in } \Omega_0^{(i)} \times [0, t^E], \\
-\nabla_{\mathbf{X}} \cdot \mathbf{Q}^{(i)} + \hat{R}_0^{(i)} &= c_v^{(i)} \dot{T}^{(i)} && \text{in } \Omega_0^{(i)} \times [0, t^E], \\
(\mathbf{F}^{(i)} \mathbf{S}^{(i)}) \mathbf{N}^{(i)} &= \hat{\mathbf{t}}_0^{(i)} && \text{on } \Gamma_\sigma^{(i)} \times [0, t^E], \\
\mathbf{Q}^{(i)} \cdot \mathbf{N}^{(i)} &= \hat{Q}_0^{(i)} && \text{on } \Gamma_q^{(i)} \times [0, t^E], \\
\mathbf{u}^{(i)} &= \hat{\mathbf{u}}^{(i)} && \text{on } \Gamma_u^{(i)} \times [0, t^E], \\
T^{(i)} &= \hat{T}^{(i)} && \text{on } \Gamma_T^{(i)} \times [0, t^E], \\
\mathbf{u}^{(i)} &= \mathbf{u}_0^{(i)} && \text{in } \Omega_0^{(i)} \times 0, \\
\dot{\mathbf{u}}^{(i)} &= \dot{\mathbf{u}}_0^{(i)} && \text{in } \Omega_0^{(i)} \times 0, \\
T^{(i)} &= T_0^{(i)} && \text{in } \Omega_0^{(i)} \times 0, \\
\boldsymbol{\sigma}^{(i)} \mathbf{n}^{(i)} &= \mathbf{t}_c^{(i)} && \text{on } \gamma_c^{(i)} \times [0, t^E], \\
\mathbf{q}^{(i)} \cdot \mathbf{n}^{(i)} &= q_c^{(i)} && \text{on } \gamma_c^{(i)} \times [0, t^E],
\end{aligned} \tag{1}$$

where $(\dot{\cdot})$ is the total time derivative, $\nabla_{\mathbf{X}}$ the gradient with respect to the material position vector \mathbf{X} , $\hat{\mathbf{b}}_0^{(i)}$ the body forces per unit reference volume, $\rho_0^{(i)}$ the mass density per unit reference volume, $\hat{R}_0^{(i)}$ the heat source per unit reference volume, and $c_v^{(i)}$ the specific heat capacity. \mathbf{N} and \mathbf{n} represent outward unit-normal vectors onto the surfaces of the considered bodies in material and spatial description, respectively. Furthermore, \mathbf{F} , \mathbf{S} , $\boldsymbol{\sigma}$, \mathbf{Q} , and \mathbf{q} are the deformation gradient, second Piola–Kirchhoff stress tensor, Cauchy stress tensor, material heat flux, and spatial heat flux, respectively, and are detailed in the following sections. Here the first two equations are the momentum balance and the heat conduction equation, respectively. The Neumann boundary conditions for the mechanical problem on $\Gamma_\sigma^{(i)}$ and for the thermal problem on $\Gamma_q^{(i)}$ involve the prescribed fluxes $\hat{\mathbf{t}}_0^{(i)}$ and $\hat{Q}_0^{(i)}$. The Dirichlet boundary conditions for the mechanical problem on $\Gamma_u^{(i)}$ and for the thermal problem on $\Gamma_T^{(i)}$ are represented by the prescribed values $\hat{\mathbf{u}}^{(i)}$ and $\hat{T}^{(i)}$, respectively. $\mathbf{u}_0^{(i)}$, $\dot{\mathbf{u}}_0^{(i)}$, and $T_0^{(i)}$ depict the initial conditions of the displacement, velocity, and temperature, respectively. Finally, the last two equations correspond to the Cauchy traction $\mathbf{t}_c^{(i)}$ and Cauchy heat flux $q_c^{(i)}$ at the contact surfaces $\gamma_c^{(i)}$.

For the subsequent finite element formulation, first the weak forms of the coupled thermo-mechanical IBVP is formulated. The weak forms are obtained by multiplying the linear momentum and heat conduction equations in (1) with test functions $\delta \mathbf{u}^{(i)}$ and $\delta T^{(i)}$, respectively, then integrating over the domains and followed by application of Green's theorem. The mechanical and thermal weak form without contact contribution reads

$$\underbrace{\int_{\Omega^{(i)}} \rho_0^{(i)} \delta \mathbf{u}^{(i)} \cdot \ddot{\mathbf{u}}^{(i)} \, d\Omega}_{\delta \mathcal{W}_u^{\text{iner}}} + \underbrace{\int_{\Omega^{(i)}} \nabla_{\mathbf{X}} \delta \mathbf{u}^{(i)} : (\mathbf{F}^{(i)} \mathbf{S}^{(i)}) \, d\Omega}_{\delta \mathcal{W}_u^{\text{int}}} - \underbrace{\left(\int_{\Omega^{(i)}} \delta \mathbf{u}^{(i)} \cdot \hat{\mathbf{b}}_0^{(i)} \, d\Omega + \int_{\Gamma_\sigma^{(i)}} \delta \mathbf{u}^{(i)} \cdot \hat{\mathbf{t}}_0^{(i)} \, d\Gamma \right)}_{\delta \mathcal{W}_u^{\text{ext}}} = 0 \tag{2}$$

$$\text{and } \underbrace{\int_{\Omega^{(i)}} \delta T^{(i)} c_v^{(i)} \dot{T}^{(i)} \, d\Omega}_{\delta \mathcal{W}_T^{\text{iner}}} + \underbrace{\int_{\Omega^{(i)}} \nabla_{\mathbf{X}} \delta T^{(i)} \cdot \mathbf{Q}^{(i)} \, d\Omega}_{\delta \mathcal{W}_T^{\text{int}}} - \underbrace{\left(\int_{\Omega^{(i)}} \delta T^{(i)} \hat{R}_0^{(i)} \, d\Omega + \int_{\Gamma_q^{(i)}} \delta T^{(i)} \hat{Q}_0^{(i)} \, d\Gamma \right)}_{\delta \mathcal{W}_T^{\text{ext}}} = 0, \tag{3}$$

respectively, wherein the $\delta \mathcal{W}_u^{\text{iner}}$, $\delta \mathcal{W}_u^{\text{int}}$, and $\delta \mathcal{W}_u^{\text{ext}}$ are the mechanical inertia, internal, and external virtual works, respectively and the corresponding virtual works in thermal problem are denoted by $\delta \mathcal{W}_T^{\text{iner}}$, $\delta \mathcal{W}_T^{\text{int}}$, and $\delta \mathcal{W}_T^{\text{ext}}$.

2.2 Kinematics and constitutive model for large deformation thermo-mechanical problem

The mesh adaptation method proposed in Section 3 is motivated by one of our current research questions involving material behavior with extreme volume expansion. Since the proposed mesh adaption scheme is independent of the specific form of the material law, and also for reasons of confidentiality, the constitutive law governing the inelastic volume expansion will be stated in a generic form below.

Following the framework of nonlinear continuum mechanics, the local deformation at a material point \mathbf{X} is described by the deformation gradient $\mathbf{F} = \frac{\partial \mathbf{x}}{\partial \mathbf{X}}$. To account for inelastic deformations, we adopt the multiplicative split of the deformation gradient into an elastic part \mathbf{F}_e and an inelastic part \mathbf{F}_{in} as proposed by Lee [23] in the context of plasticity:

$$\mathbf{F} = \mathbf{F}_e \mathbf{F}_{in}. \quad (4)$$

We allow for an anisotropic inelastic volume expansion with respect to the principal stretch directions \mathbf{N}_{CG}^i , which are given by the eigenvectors of the right Cauchy–Green stretch tensor $\mathbf{C} = \mathbf{F}^T \mathbf{F}$, according to

$$\mathbf{F}_{in} = \sum_{i=1}^3 \lambda_{in}^i \mathbf{N}_{CG}^i \otimes \mathbf{N}_{CG}^i, \quad (5)$$

where λ_{in}^i is the magnitude of the inelastic expansion in the direction \mathbf{N}_{CG}^i , governed by an evolution equation

$$\dot{\lambda}_{in}^i = \dot{\lambda}_{in}^i(T, \mathbf{S}, \alpha), \quad (6)$$

accounting for dependencies of the inelastic volume expansion on the current temperature, stress state and on the scalar-valued internal variable α governing the material history. Exemplarily, the scalar α can be a material degradation factor which reduces from 1 to 0 when the expansion process is complete. In the numerical examples studied in this work, we prescribe α as an explicit function of time. Models that are similar to the aforementioned approach have been introduced, e.g., in the context of biological growth [24, 25].

In analogy to the (total) right Cauchy–Green stretch tensor \mathbf{C} , the *elastic* right Cauchy–Green stretch tensor is defined as $\mathbf{C}_e = \mathbf{F}_e^T \mathbf{F}_e$. Based on \mathbf{C}_e , we define a hyperelastic strain-energy function $\Psi_e(\mathbf{C}_e)$ under the assumption that the elastic response does not explicitly depend on the temperature. Consequently, the second Piola–Kirchhoff stress tensor \mathbf{S} can be computed as (see [26] for more details)

$$\mathbf{S} = 2 \mathbf{F}_{in}^{-1} \frac{\partial \Psi_e}{\partial \mathbf{C}_e} \mathbf{F}_{in}^{-T}. \quad (7)$$

Furthermore, the spatial Cauchy stress tensor $\boldsymbol{\sigma}$ can be described as $\boldsymbol{\sigma} = (\det \mathbf{F})^{-1} \mathbf{F} \mathbf{S} \mathbf{F}^T$. In the examples presented in this paper, the hyperelastic strain-energy function is based on a Neo–Hookean model as presented in [26].

Finally, the thermal constitutive equation relating heat flux and temperature gradient via the isotropic heat conductivity k_0 is formulated on the basis of Fourier’s law. The latter can be stated using either the (material) second Piola–Kirchhoff heat flux \mathbf{Q} or the spatial heat flux $\mathbf{q} = (\det \mathbf{F})^{-1} \mathbf{F} \mathbf{Q}$ according to

$$\mathbf{Q} = -k_0 \mathbf{C}^{-1} \nabla_{\mathbf{X}} T \quad \text{or} \quad \mathbf{q} = -\frac{k_0}{\det \mathbf{F}} \nabla_{\mathbf{x}} T, \quad (8)$$

where we distinguish between the material gradient $\nabla_{\mathbf{X}} = \frac{\partial}{\partial \mathbf{X}}$ and the spatial gradient $\nabla_{\mathbf{x}} = \frac{\partial}{\partial \mathbf{x}}$.

2.3 Thermo-mechanical contact

In this section, we discuss the thermo-mechanical contact formulation used in this work. While the general formulation accounts for frictional contact interaction, only the frictionless case is considered in the subsequent numerical examples. The underlying contact constraints along with the basics of mortar methods for constraint enforcement and regularization are briefly summarized below. For a detailed description of these mortar methods in the context of mechanical or thermo-mechanical contact interaction, the interested reader is referred to [27, 28, 29] and [30, 31], respectively.

2.3.1 Mechanical contact problem: Kinematics and contact forces

In the following, we distinguish the contacting surfaces as master and slave side denoted by the sets \mathcal{M} and \mathcal{S} , respectively. Here, a superscript (1) refers to the slave side and $\gamma_c^{(1)}$ represents the contact surface on the slave side. The relative motion between these interfaces at any time instant t is quantified by the smooth mapping (see Figure 1)

$$\chi_t(\mathbf{x}^{(1)}) : \gamma_c^{(1)} \rightarrow \gamma_c^{(2)}, \mathbf{x}^{(1)} \mapsto \mathbf{x}^{(2)}. \quad (9)$$

This mapping projects any point $\mathbf{x}^{(1)}$ from the slave surface $\gamma_c^{(1)}$ onto the master surface $\gamma_c^{(2)}$ along the outward normal $\mathbf{n}(\mathbf{x}^{(1)})$ or in short \mathbf{n} (see Figure 1). The unit vectors spanning the tangential plane at the contact point are denoted as $\boldsymbol{\tau}^\eta$ and $\boldsymbol{\tau}^\xi$. The mapping is assumed to exist in the zone of closed contact and its close vicinity. For (potentially) interacting points on the slave surface $\gamma_c^{(1)}$, the normal gap is defined as

$$g_n(\mathbf{x}^{(1)}) = -\mathbf{n} \cdot [\mathbf{x}^{(1)} - \mathbf{x}^{(2)}]. \quad (10)$$

Moreover, the traction vectors acting on the contact surfaces are denoted as $\mathbf{t}_c^{(i)}$. Based on a balance of linear momentum, the traction vectors on the slave and master side of the contact surface are related according to $\mathbf{t}_c^{(1)} = -\mathbf{t}_c^{(2)} =: \mathbf{t}_c$. Furthermore, the contact traction can be decomposed into a normal $p_n^{(i)}$ and a tangential component $\mathbf{t}_\tau^{(i)}$ according to

$$p_n^{(i)} = \mathbf{n} \cdot \mathbf{t}_c^{(i)}, \quad (11)$$

$$\mathbf{t}_\tau^{(i)} = (\mathbf{I} - \mathbf{n} \otimes \mathbf{n})\mathbf{t}_c^{(i)}. \quad (12)$$

2.3.2 Mechanical contact problem: Constraints and virtual work

The (frictionless) mechanical contact constraints are given by Hertz–Signorini–Moreau conditions:

$$g_n \geq 0, \quad p_n \leq 0, \quad p_n g_n = 0 \quad \text{on } \gamma_c^{(1)}. \quad (13)$$

As basis for a variational statement of the contact problem, the slave side traction vector \mathbf{t}_c is introduced as an additional primary field, which is identified as Lagrange multiplier $\boldsymbol{\lambda}_c = -\mathbf{t}_c$ associated with the contact constraint. If the normal component of the Lagrange multiplier is denoted as $\lambda_{c,n} = \mathbf{n} \cdot \boldsymbol{\lambda}_c$, the contact virtual work can be shown to yield:

$$\delta \mathcal{W}_u^c = - \int_{\gamma_c^{(1)}} \llbracket \delta \mathbf{u} \rrbracket \cdot \boldsymbol{\lambda}_c \, d\gamma = \int_{\gamma_c^{(1)}} \delta g_n \lambda_{c,n} \, d\gamma, \quad (14)$$

where $\llbracket \cdot \rrbracket = (\cdot)^{(1)} - [(\cdot)^{(2)} \circ \chi_t]$ is the jump operator (cf. (9)) and δg_n the variation of the normal gap in (10).

2.3.3 Thermal contact problem

Next, the thermal effects at the contacting surfaces have to be addressed. The heat balance at the interface reads

$$q_c^{(1)} + q_c^{(2)} = 0, \quad (15)$$

with $q_c^{(1)}$ and $q_c^{(2)}$ being the slave and master side heat fluxes across the contact interface defined according to

$$q_c^{(i)} = \mathbf{q}^{(i)} \cdot \mathbf{n}^{(i)}. \quad (16)$$

Within this work, an interface heat flux model with a linear dependence on the contact pressure is used according to

$$q_c^{(1)} = \beta_c |p_n| \llbracket T \rrbracket, \quad q_c^{(2)} = -\beta_c |p_n| \llbracket T \rrbracket, \quad (17)$$

where $\beta_c \geq 0$ is the contact heat conductivity. Finally, the virtual work of the interface heat conduction problem reads:

$$\delta \mathcal{W}_T^c = - \int_{\gamma_c^{(1)}} q_c^{(1)} \llbracket \delta T \rrbracket \, d\gamma, \quad (18)$$

Therein, all contact integrals are transformed into pure slave side integrals using (9). As studied in [32, 33, 34], it is not necessary to introduce thermal Lagrange multipliers $\lambda_T = -q_c^{(1)}$ to enforce the thermal interface constraints. Instead, a direct substitution of the heat flux model (17) into (18) allows to express the interface heat fluxes as function of the temperature, which is the primary variable of the thermal problem.

Remark 2.3.1. *The drawback of this direct heat flux substitution method is that the problem becomes ill-conditioned for very large values of β_c , i.e., in the limit $\beta_c \rightarrow \infty$. In this case, alternative approaches such as the Lagrange multiplier method [31] or Nitsche's method [35] are well suited.*

2.4 Discretization in space and time

The displacement and temperature field are approximated in space using discrete nodal values \mathbf{d}_j and \mathbf{T}_j and ansatz functions N_j , whereas the Lagrange multiplier field is approximated using nodal value $\boldsymbol{\Lambda}_{c,j}$ and ansatz functions ϕ_j , viz

$$\mathbf{u}^h = \sum_{j=1}^n N_j \mathbf{d}_j, \quad T^h = \sum_{j=1}^n N_j \mathbf{T}_j, \quad \boldsymbol{\lambda}_c^h = \sum_{j \in \mathcal{S}} \phi_j \boldsymbol{\Lambda}_{c,j}. \quad (19)$$

In (19) the global vectors \mathbf{d} and \mathbf{T} contain all displacement and temperature degrees of freedom, respectively and the vector $\boldsymbol{\Lambda}_c$ all nodal Lagrange multipliers. The corresponding test functions can be written as

$$\delta \mathbf{u}^h = \sum_{j=1}^n N_j \delta \mathbf{d}_j, \quad \delta T^h = \sum_{j=1}^n N_j \delta \mathbf{T}_j, \quad \delta \boldsymbol{\lambda}_c^h = \sum_{j \in \mathcal{S}} \phi_j \delta \boldsymbol{\Lambda}_{c,j}. \quad (20)$$

The ansatz functions N_j can be any Lagrange polynomials for classical finite elements and ϕ_j be any Lagrange multiplier shape function as demonstrated in [29, 36].

Now the semi-discrete solid mechanics problem can be obtained by substituting (19)_{1,3} and (20)_{1,3} into the weak form (2) as:

$$\mathbf{M}_u \ddot{\mathbf{d}} + \mathbf{f}_u^{\text{int}}(\mathbf{d}, \mathbf{T}) - \mathbf{f}_u^{\text{ext}} + \mathbf{f}_u^c = \mathbf{0}, \quad (21)$$

where \mathbf{M}_u represents the constant mass matrix and $\mathbf{M}_u \ddot{\mathbf{d}}$ corresponds to discretized inertia virtual work $\delta \mathcal{W}_u^{\text{iner}}$, $\mathbf{f}_u^{\text{int}}$ is the internal force and corresponds to $\delta \mathcal{W}_u^{\text{int}}$, while the external force is denoted by $\mathbf{f}_u^{\text{ext}}$ and corresponds to $\delta \mathcal{W}_u^{\text{ext}}$. Lastly, \mathbf{f}_u^c in (21) is the contact force which is the discretized contact virtual work (14) and given as

$$\mathbf{f}_u^c = [\mathbf{0}, -\mathbf{M}(\mathbf{d}), \mathbf{D}(\mathbf{d})]^T \boldsymbol{\Lambda}_c, \quad (22)$$

where \mathbf{D} and \mathbf{M} are the well-known mortar matrices. (22) is obtained after rearranging the displacement vector in a set of inactive \mathcal{I} , master \mathcal{M} , and slave \mathcal{S} degrees of freedom.

The spatial discretization of the mechanical problem is only complete with the discretization of the contact constraints (13). The constraints are discretized using the Lagrange multiplier ansatz function ϕ_j (19)₃ and read as

$$\tilde{g}_{n,j} := \int_{\gamma_c^{(1),h}} \phi_j g_n^h \, d\gamma \geq 0, \quad \lambda_{c,n,j} \leq 0, \quad \lambda_{c,n,j} \tilde{g}_{n,j} = 0 \quad \forall j \in \mathcal{S} \quad \text{on} \quad \gamma_c^{(1)}, \quad (23)$$

where $\tilde{g}_{n,j}$ is referred to as weighted gap (see [29]).

To enforce the normal contact constraint (23), we employ the penalty regularization as detailed in [29]. Wherein the contact pressure $\lambda_{c,n}$ and weighted gap \tilde{g}_n at every slave node j is regularized by introducing a penalty parameter $0 < \epsilon_c < \infty$ as

$$\lambda_{c,n,j} = \epsilon_c \langle -\tilde{g}_{n,j} \rangle, \quad (24)$$

where $\langle \cdot \rangle$ denotes the Macauley bracket. As a consequence of regularization the Lagrange multipliers are no longer a primary variable; for a comprehensive treatment of penalty regularized mortar finite element methods, the interested reader is referred to [37, 38].

Remark 2.4.1. *The choice of the penalty parameter affects the accuracy of the contact problem. To circumvent large/significant penetration due to lower penalty and an artificial gap as well as ill-conditioning due to higher penalty parameter, an adaptive penalty parameter scaling can be employed as in [35].*

The semi-discrete thermal problem is achieved by substituting (19)₂ and (20)₂ in (3) and reads:

$$\mathbf{M}_T \dot{\mathbf{T}} + \mathbf{f}_T^{\text{int}}(\mathbf{d}, \mathbf{T}) - \mathbf{f}_T^{\text{ext}} + \mathbf{f}_T^c = \mathbf{0}, \quad (25)$$

where \mathbf{M}_T is the constant heat capacity matrix, $\mathbf{f}_T^{\text{int}}$, $\mathbf{f}_T^{\text{ext}}$, and \mathbf{f}_T^c are the thermal internal, external, and contact forces, respectively. In (25), $\mathbf{M}_T \dot{\mathbf{T}}$, $\mathbf{f}_T^{\text{int}}$, $\mathbf{f}_T^{\text{ext}}$, and \mathbf{f}_T^c correspond to the discretized virtual works $\delta \mathcal{W}_T^{\text{iner}}$, $\delta \mathcal{W}_T^{\text{int}}$, $\delta \mathcal{W}_T^{\text{ext}}$, and $\delta \mathcal{W}_T^c$, respectively. For simplicity, the external forces ($\mathbf{f}_u^{\text{ext}}$ and $\mathbf{f}_T^{\text{ext}}$) are assumed to be independent of the displacement and temperature field.

Next, the temporal discretization of the solid dynamics problem is achieved via so-called generalized- α scheme. The discrete solid mechanics problem for the time interval $[t^n, t^{n+1}]$ with step Δt reads

$$\mathbf{r}_u(\mathbf{d}^{n+1}, \mathbf{T}^{n+1}) = \mathbf{M}_u \dot{\mathbf{d}}^{n+1-\alpha_{u,M}} + \mathbf{f}_u^{\text{int},n+1-\alpha_{u,f}} - \mathbf{f}_u^{\text{ext},n+1-\alpha_{u,f}} + \mathbf{f}_u^{c,n+1} = \mathbf{0}, \quad (26)$$

where the superscript $n+1-\alpha_{u,(\cdot)}$ denotes the quantities evaluated at generalized mid-point of the time interval with respective generalized- α parameters $\alpha_{u,(\cdot)}$ more details see e.g. [36, 39]. In (26), all the terms except $\mathbf{f}_u^{\text{int},n+1-\alpha_{u,f}}$ and $\mathbf{f}_u^{c,n+1}$ are standard formulations as in, e.g. [31, 29]. The value at the generalized mid-point is obtained by linearly combining the values at t^n and t^{n+1} , e.g. $\mathbf{f}_u^{\text{int},n+1-\alpha_{u,f}} = (1-\alpha_{u,f})\mathbf{f}_u^{\text{int},n+1} + \alpha_{u,f}\mathbf{f}_u^{\text{int},n}$. Contrarily, the contact force \mathbf{f}_u^c is computed at t^{n+1} to avoid any unwanted energy addition to the discrete system in the event of change in active contact surface as stated in [31]. The evaluation of deformation gradient, elastic right Cauchy–Green tensor and stress tensor to compute the internal force $\mathbf{f}_u^{\text{int},n+1}$ from $\delta \mathcal{W}_u^{\text{int}}$ is as follows. The total deformation gradient is given as

$$\mathbf{F}^{n+1} = \mathbf{F}_e^{n+1} \mathbf{F}_{in}^{n+1}, \quad (27)$$

where the inelastic deformation gradient \mathbf{F}_{in}^{n+1} at t^{n+1} is approximated according to

$$\mathbf{F}_{in}^{n+1} = \sum_{i=1}^3 \lambda_{in}^{i,n+1} \mathbf{N}_{CG}^{i,n} \otimes \mathbf{N}_{CG}^{i,n}, \quad (28)$$

where the magnitude of the inelastic expansion is found by explicit time integration of the corresponding rate equation (6) using an explicit Euler scheme, i.e., $\lambda_{in}^{i,n+1} = \lambda_{in}^{i,n} + \dot{\lambda}_{in}^{i,n} \Delta t$. Here, $\mathbf{N}_{CG}^{i,n}$ is computed from the spectral decomposition of \mathbf{C}^n . The elastic deformation gradient is computed as $\mathbf{F}_e^{n+1} = (\mathbf{F}_{in}^{n+1})^{-1} \mathbf{F}^{n+1}$. The right Cauchy–Green tensor is determined as

$$\mathbf{C}_e^{n+1} = (\mathbf{F}_e^{n+1})^T \mathbf{F}_e^{n+1}. \quad (29)$$

Lastly, the second Piola–Kirchhoff stress tensor is computed as

$$\mathbf{S}^{n+1} = 2(\mathbf{F}_{in}^{n+1})^{-1} \frac{\partial \Psi_e(\mathbf{C}_e^{n+1})}{\partial \mathbf{C}_e^{n+1}} (\mathbf{F}_{in}^{n+1})^{-T}. \quad (30)$$

Similarly, the fully discrete thermal problem via generalized- α scheme can be written as

$$\mathbf{r}_T(\mathbf{d}^{n+1}, \mathbf{T}^{n+1}) = \mathbf{M}_T \dot{\mathbf{T}}^{n+\alpha_{T,M}} + \mathbf{f}_T^{\text{int},n+\alpha_{T,f}} - \mathbf{f}_T^{\text{ext},n+\alpha_{T,f}} + \mathbf{f}_T^{c,n+\alpha_{T,f}} = \mathbf{0}, \quad (31)$$

at generalized mid-point $n + \alpha_{T,(\cdot)}$ and again obtained by appropriate linear combination of the end-point values, e.g. $\mathbf{f}_T^{\text{int},n+\alpha_{T,f}} = \alpha_{T,f} \mathbf{f}_T^{\text{int},n+1} + (1 - \alpha_{T,f}) \mathbf{f}_T^{\text{int},n}$.

Finally, the solution of the coupled non-linear problem (26) and (31) is found in a monolithic manner using the classical Newton–Raphson method with consistent linearization. The linearized system is solved using iterative solvers using preconditioners such as AMG(BGS) as studied in [39, 40].

3 Mesh adaptation

The proposed mesh adaptation consists of two steps: mesh refitting and subsequent data transfer. In the mesh refitting step we construct a "new mesh" with improved quality compared to the "old mesh". The "old mesh" is the starting point of this procedure and usually exhibits heavily distorted elements, i.e., a low mesh quality. In the second step, the associated data, e.g., nodal primary variables and history variables of the material model defined at quadrature points, is transferred from the old mesh to the new one. These two steps are described in the following. All methods presented throughout this article, are implemented in our in-house parallel multi-physics research code BACI [41].

3.1 Mesh refitting

The objective of the mesh refitting (MR) step is to achieve high-quality elements which are less distorted while preserving the topology of the boundary, i.e., the total volume of the domain. Thereto, we define an element distortion potential and solve for the minimum of this potential during the mesh refitting step, thus minimizing the distortion of the finite element mesh. As mentioned before, an additional requirement for the MR step is the preservation of the boundary topology, which requires to prohibit motion of boundary nodes in the direction normal to the boundary of the problem. However, motion of the boundary nodes should be permitted in tangential direction to allow for an optimal mesh relaxation also in the domains close to the boundary. This aspect is crucial for problems involving interface phenomena such as contact mechanics, which often result in a strong mesh distortion at the boundaries of the interacting bodies. These two requirements, i.e., prohibiting the normal displacement component while allowing free tangential movement for boundary nodes will be fulfilled by employing a novel mortar mesh sliding approach.

In the following, the mortar mesh sliding approach (Section 3.1.1) is presented, followed by the definition of the element distortion potential Section 3.1.2. Finally, in Section 3.1.3, the complete description of the MR problem is given.

3.1.1 Mesh sliding approach

Mesh sliding denotes a relative motion at the interface of two meshes that allows for free tangential sliding without detachment. To formulate such a constraint, the two bodies in Figure 1 shall be considered, which are initially in contact. To enforce non-detachment, the normal gap has to remain zero during the motion, i.e.,

$$g_n = 0. \quad (32)$$

Since no resistance with respect to tangential relative motion shall be applied, the tangential component of the interface traction vector has to vanish, similar to the friction-less contact scenario discussed before:

$$\mathbf{t}_\tau \cdot \boldsymbol{\tau} = 0. \quad (33)$$

Identical to the mechanical contact case in Section 2.3, the contribution of the mesh sliding constraint to the virtual work of the mesh refitting problem in terms of the Lagrange multiplier λ_m can be written as:

$$\delta\mathcal{W}_u = - \int_{\gamma_c^{(1)}} [[\delta\mathbf{u}]] \cdot \boldsymbol{\lambda}_m \, d\gamma = \int_{\gamma_c^{(1)}} \delta g_n \lambda_{m,n} \, d\gamma = 0, \quad (34)$$

where the normal component of the Lagrange multiplier is $\lambda_{m,n} = \boldsymbol{\lambda}_m \cdot \mathbf{n}$. Following the mortar finite element formulation presented above, the spatially discretized mesh sliding force vector \mathbf{f}_u^m is identical to the vector \mathbf{f}_u^c in (22). The only difference between the mesh sliding approach and the friction-less contact case presented above is given through the constraints (13) and (32), where the former represents an inequality constraint and the latter an equality constraint.

Finally, the mesh sliding constraints are enforced through a regularization based on the discretized weighted nodal gap $\tilde{g}_{n,j}$ (see (23)₁) and a penalty parameter $0 < \epsilon_m < \infty$, which eventually yields for node j :

$$\lambda_{m,n,j} = \boldsymbol{\lambda}_{m,j} \cdot \mathbf{n}_j = -\epsilon_m \tilde{g}_{n,j}, \quad \boldsymbol{\lambda}_{m,j} \cdot \boldsymbol{\tau}_j = 0 \quad \forall j \in \mathcal{S}. \quad (35)$$

The significant difference between the penalty regularization of the mesh sliding (35) and the mechanical contact (24) is the Macaulay brackets. They must be used in contact mechanics because contact forces only exist if the gap is negative. In contrast, in mesh sliding, the forces exist regardless of the sign of the gap to prevent penetration and detachment.

3.1.2 Element distortion potential

Generally, mesh quality can be measured in geometric quantities such as skewness and aspect ratio. The skewness quantifies the angles enclosed by the element faces or edges, whereas the aspect ratio measures the ratio of the dimensions of elements in different spatial directions. In this work, we control the element size and aspect ratio by enforcing constraints on the element edge lengths, denoted as G_E , and the skewness by enforcing constraints on the angles enclosed by the element edges, denoted as G_A .

We demonstrate the formulation of these constraints using an 8-noded hexahedral element, which is the finite element type employed in the numerical examples of this work. As shown in Figure 2, we first define 12 edge vectors \mathbf{v}_j^i . Here, the superscript $i \in \{1, 2, 3\}$ denotes the direction \mathbf{e}^i associated with the orientation of the edge in parameter space. The subscript $j \in \{1, 2, 3, 4\}$ represents a counting index for the four individual edge vectors pointing to a given direction i . As illustrated in Figure 2, each edge vector is defined as the difference vector between the (current) spatial position vectors of the two nodes associated with the edge vector. From these individual edge vectors, an averaged edge vector $\bar{\mathbf{v}}^i$ is defined as

$$\bar{\mathbf{v}}^i = \frac{1}{4} \sum_{j=1}^4 \mathbf{v}_j^i. \quad (36)$$

Based on these definitions, the edge and angle constraints will be formulated in the following.

Edge constraints G_E^i

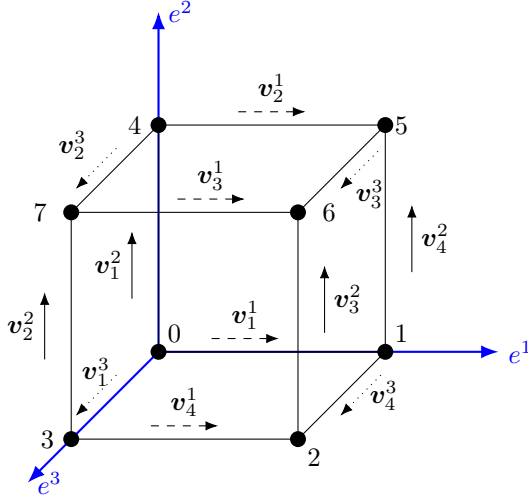
To impose specific edge lengths on elements, we apply constraints on both, the average edge vectors $\bar{\mathbf{v}}^i$ and the individual edge vectors \mathbf{v}_j^i , which are denoted as \bar{G}_E^i and \hat{G}_E^i , respectively. The constraint \bar{G}_E^i on the average edge vector in direction \mathbf{e}^i is defined as

$$\bar{G}_E^i = \frac{\sqrt{\bar{\mathbf{v}}^i \cdot \bar{\mathbf{v}}^i}}{l_r^i} - 1 \stackrel{!}{=} 0, \quad (37)$$

with l_r^i denoting a target element edge length in direction \mathbf{e}^i to be prescribed. This constraint enforces the length l_r^i on the average edge vector $\bar{\mathbf{v}}^i$. In a next step, the constraint \hat{G}_E^i is defined according to

$$(\hat{G}_E^i)_j = \frac{\mathbf{v}_j^i \cdot \mathbf{v}_j^i}{\bar{\mathbf{v}}^i \cdot \bar{\mathbf{v}}^i} - 1 \stackrel{!}{=} 0, \quad (38)$$

which enforces that each individual edge vector equals the associated average edge vector. Prescribing a spatial distribution function for the element size will be called *mesh localization* throughout this work. It can be achieved by prescribing spatial functions for the target lengths, i.e., $l_r^i = l_r^i(\mathbf{X})$. To sum up, so far we have defined 15 constraints associated with element size and aspect ratio, 3 on the average edge vectors and 12 on the individual edge vectors.



$$\begin{aligned}
\mathbf{v}_{\{1,2,3,4\}}^1 &= \mathbf{x}_{\{1,5,6,2\}} - \mathbf{x}_{\{0,4,7,3\}} \\
\mathbf{v}_{\{1,2,3,4\}}^2 &= \mathbf{x}_{\{4,7,6,5\}} - \mathbf{x}_{\{0,3,2,1\}} \\
\mathbf{v}_{\{1,2,3,4\}}^3 &= \mathbf{x}_{\{3,7,6,2\}} - \mathbf{x}_{\{0,4,5,1\}}
\end{aligned}$$

Figure 2: Illustration of edge vectors defined to formulate included angle and edge constraints for a hexahedral element.

Angle constraints G_A^{mn}

Next, we construct angle constraints considering the angle enclosed by a pair of edge vectors \mathbf{v}_j^i with common initial point. For example, the angle constraints G_A^{mn} for node "0" are formulated as (c.f. Figure 2)

$$\begin{aligned}
G_A^{12} &= \frac{\mathbf{v}_1^1 \cdot \mathbf{v}_1^2}{\|\mathbf{v}_1^1\| \|\mathbf{v}_1^2\|} - \cos \theta_r^{12} \stackrel{!}{=} 0, \\
G_A^{13} &= \frac{\mathbf{v}_1^1 \cdot \mathbf{v}_1^3}{\|\mathbf{v}_1^1\| \|\mathbf{v}_1^3\|} - \cos \theta_r^{13} \stackrel{!}{=} 0, \\
G_A^{23} &= \frac{\mathbf{v}_1^2 \cdot \mathbf{v}_1^3}{\|\mathbf{v}_1^2\| \|\mathbf{v}_1^3\|} - \cos \theta_r^{23} \stackrel{!}{=} 0,
\end{aligned} \tag{39}$$

where θ_r^{12} , θ_r^{13} , and θ_r^{23} are the enclosed target angles to achieve. To achieve perpendicular edges, we set $\theta_r^{12} = \theta_r^{13} = \theta_r^{23} = \pi/2$. Likewise, angle constraints can be formulated for all remaining nodes. To conclude, we have formulated 24 angular constraints in total.

Constraint enforcement

Finally, we enforce these constraints on basis of a distortion potential with penalty parameters $\bar{\varepsilon}_E$, $\hat{\varepsilon}_E$ and ε_A given as

$$\pi_d = \frac{1}{2} \bar{\varepsilon}_E \sum_{i=1}^{ndir} \bar{G}_E^i \bar{G}_E^i + \frac{1}{2} \hat{\varepsilon}_E \sum_{i=1}^{ndir} \sum_{j=1}^4 (\hat{G}_E^i)_j (\hat{G}_E^i)_j + \frac{1}{2} \varepsilon_A \sum_{n=1}^{nnode} (G_A^{12} G_A^{12} + G_A^{13} G_A^{13} + G_A^{23} G_A^{23})_n, \tag{40}$$

where $ndir = 3$ is the number of spatial directions and $nnode = 8$ is the number of nodes. In the following, the meaning of the different constraint contributions shall be briefly discussed. Clearly, the constraints \hat{G}_E^i penalize deviations of the individual edge lengths from the average edge length in a given direction, i.e., they enforce the element shape to equal a parallelepiped in the limit of $\hat{\varepsilon}_E \rightarrow \infty$. If additionally also the angular constraints G_A with target angles $\theta_r^{12} = \theta_r^{13} = \theta_r^{23} = \pi/2$ are enforced, the element will tend towards a cuboid shape. Eventually, if equal target lengths are chosen for the constraints \bar{G}_E^i , i.e., $l_r^1 = l_r^2 = l_r^3 =: l_r$, the element will approach a cubic shape. Finally, the absolute value of l_r determines how a shape-preserving scaling of the element size will be penalized. For example, by choosing l_r as the initial edge length of a regular mesh with cubic elements, every (even shape-preserving) deviation from the initial element size will be penalized. Clearly, the chosen set of 15 + 24 constraints per element is redundant, since an hexahedral element with 8 nodes only exhibits 24 degrees of freedom (including 6 rigid body modes changing neither the shape nor the size of the element). However, this over-constraining is no problem when employing a penalty potential for constraint enforcement. Moreover, this specific choice of (redundant) constraints allows to independently control different modes of element distortion (with different effect on the mesh quality), as elaborated above. In addition, the chosen set of constraints leads to a distortion potential that is symmetric with respect to the node numbering, i.e., the result will not change if the node numbering is changed for a given mesh. In conclusion, it is emphasized that the

definition of an element distortion potential is not unique. The specific choice presented above has proven effective in the numerical test cases we have investigated so far. In particular, the specification $\bar{\varepsilon}_E = \hat{\varepsilon}_E =: \varepsilon_E$ turned out as a robust choice and will be used in the remainder of this work.

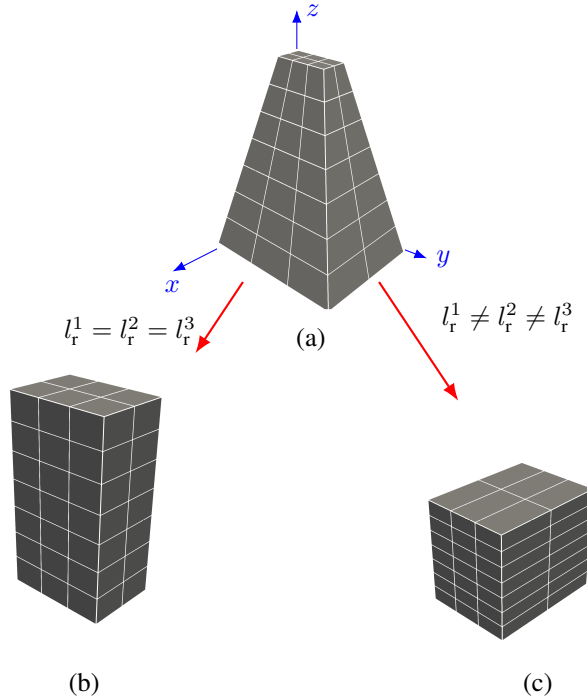


Figure 3: Illustration of constraints: (a) initial geometry (b) resulting geometry when elemental constraints with $l_r^1 = l_r^2 = l_r^3$ and $\theta_r^{mn} = \pi/2$ are applied on (a), and (c) when $l_r^1 \neq l_r^2 \neq l_r^3$ with $\theta_r^{mn} = \pi/2$ are applied on (a).

Demonstration example: Effect of target element edge lengths

To conclude this section, the effect of the element constraints shall be demonstrated using the numerical example shown in Figure 3. Consider the truncated rectangular pyramid-shaped body in Figure 3a meshed with 42 hexahedral elements. The body is freely supported in the first quadrant, so that rigid body modes are suppressed and a stress-free volume change is permitted. We apply the constraints in (40) with equal target lengths (see (37)) in all directions, i.e. $l_r^1 = l_r^2 = l_r^3$ and $\theta_r^{mn} = \pi/2$. The resulting geometry is shown in Figure 3b. As expected the obtained geometry is rectangular with cubic elements. When $l_r^1 \neq l_r^2 \neq l_r^3$ and $\theta_r^{mn} = \pi/2$ the resulting geometry remains rectangular and contains rectangular elements as illustrated in Figure 3c. This shows that the suggested approach is suitable to obtain elements of a specific desired shape. It is emphasized that this example has been designed to visualize the isolated effect of the element distortion potential without imposing mesh sliding constraints at the boundaries. Thus, in contrast to actual mesh refitting problems, the mesh in this demonstration example is not required to preserve the boundary contour of the discretized body.

3.1.3 Problem description of mesh refitting method

Let the old mesh be defined on the domain $\Omega_m \subset \Omega_t$ with boundary $\Gamma_m^{(1)} := \partial\Omega_m$. We apply the mesh sliding approach from above (see Section 3.1.1) to preserve the boundary contour of a given body while allowing for tangential sliding. This will be done only for the boundary nodes without prescribed Dirichlet boundary condition, i.e., only for nodes on the boundary $\Gamma_m^{(1)} \setminus \Gamma_u$. From a technical point of view, to enable the mesh sliding approach in the same sense as typical for mortar interface problems, we replicate the discretized boundary $\Gamma_m^{(1)}$ and denote this auxiliary boundary as $\Gamma_m^{(2)}$ (see Figure 4). Since $\Gamma_m^{(2)}$ and $\Gamma_m^{(1)}$ coincide, a one-to-one mapping between the nodes on these boundaries exists, i.e., nodal positions can be transferred in a straight-forward manner from $\Gamma_m^{(1)}$ to $\Gamma_m^{(2)}$. It is emphasized that the auxiliary boundary $\Gamma_m^{(2)}$ is only required to represent a fictitious interaction partner to apply the standard mesh-sliding method to the boundary nodes of the original mesh on $\Gamma_m^{(1)}$. This means, that the nodal position and displacement values on

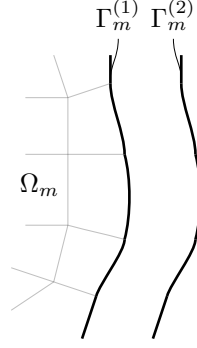


Figure 4: Illustration of mesh sliding interface surfaces with auxiliary boundary $\Gamma_m^{(2)}$.

the auxiliary boundary $\Gamma_m^{(2)}$ remain fixed, i.e., are prescribed per Dirichlet boundary condition, and the mesh-refitting problem does not need to be solved for these nodes.

The complete MR problem after solving the fully discretized thermo-mechanical problem for time step t^{n+1} is constructed as follows: First, update the reference configuration of the MR problem with the (converged) current configuration of the old mesh, i.e., $\mathbf{X}_{\Omega_m} = \mathbf{x}_{\Omega_m}^{n+1}$. This means that the current state of the old mesh becomes the reference state of the MR problem. Now, the solution of the mesh refitting problem is defined as the stationary value of the following total potential

$$\pi_d + \pi_m \rightarrow \text{stat.}, \quad (41)$$

where the element distortion potential π_d is given in (40) and π_m represents an abstract potential for constraint enforcement (e.g., a Lagrange multiplier or penalty potential) whose variation is given by the discretized form of (34). Similar to the weak form of our physical (thermo-mechanical) problem, as necessary condition for a stationary value the variation of the discrete potential (41) has to vanish, leading to the following system of nonlinear (residual) equations:

$$\mathbf{f}_u^d + \mathbf{f}_u^m = \mathbf{0}, \quad (42)$$

where $\mathbf{f}_u^d = \frac{\partial \pi_m}{\partial \mathbf{d}}$ is the gradient of the discrete element distortion potential (40) and \mathbf{f}_u^m is the nodal mesh sliding force vector according to Section 3.1.1. The solution of the non-linear system (42) is found using a Newton-Raphson scheme based on a consistent linearization.

Remark 3.1.1. *Updating the reference states of the MR problem is only done when the mesh adaptation step is performed, i.e., not in every discrete time step solved for the physical (thermo-mechanical) problem. Furthermore, the MR problem only requires the current state of the old mesh, i.e., the current nodal position vectors.*

Remark 3.1.2. *By updating the reference configuration of the MA problem with the current configuration of the old mesh the MA procedure gets more robust because the MA problem is thereby independent of the original reference configuration. The increased robustness of the MA is based on the fact that due to the update of the reference configuration the MA problem benefits from already performed MA steps earlier in the simulation and the necessary relocation is smaller for subsequent MA steps.*

Demonstration example: Influence of mesh sliding approach

Next, we demonstrate the benefits of mesh sliding using two numerical examples in Figures 5 and 6. First, consider an isothermal frictional sliding of a rigid cylinder over a rectangular block. The rigid cylinder has a diameter of 0.25 with height 0.125, and a rectangular block of dimensions $1 \times 0.25 \times 0.125$. The rectangular block is meshed with 2500 cubic 8-noded hexahedral elements and is modeled with an elasto-plastic constitutive model as presented in [42]. The isothermal frictional contact is modeled using the mortar penalty method studied in [29]. The cylinder is slightly pressed onto the rectangular block and moved a distance of 0.5 starting from the quarter length of the block. This procedure induces plastic deformation on the boundary as shown in Figure 5b. It can be seen that the boundary elements underneath and near the cylinder (shown in a red dashed circle) have experienced shear distortion. At this deformed state, the presented mesh refitting is performed and the resulting configuration is illustrated in Figure 5c. The refitted mesh in the whole domain (shown in a green dashed circle) resembles the initial uniform mesh, i.e., cubic elements. This is achieved by the free tangential sliding of the boundary nodes in the mesh refitting step. In short, in case of pure shear at the boundary, the refitted mesh is close to the initial mesh after applying the mesh sliding approach.

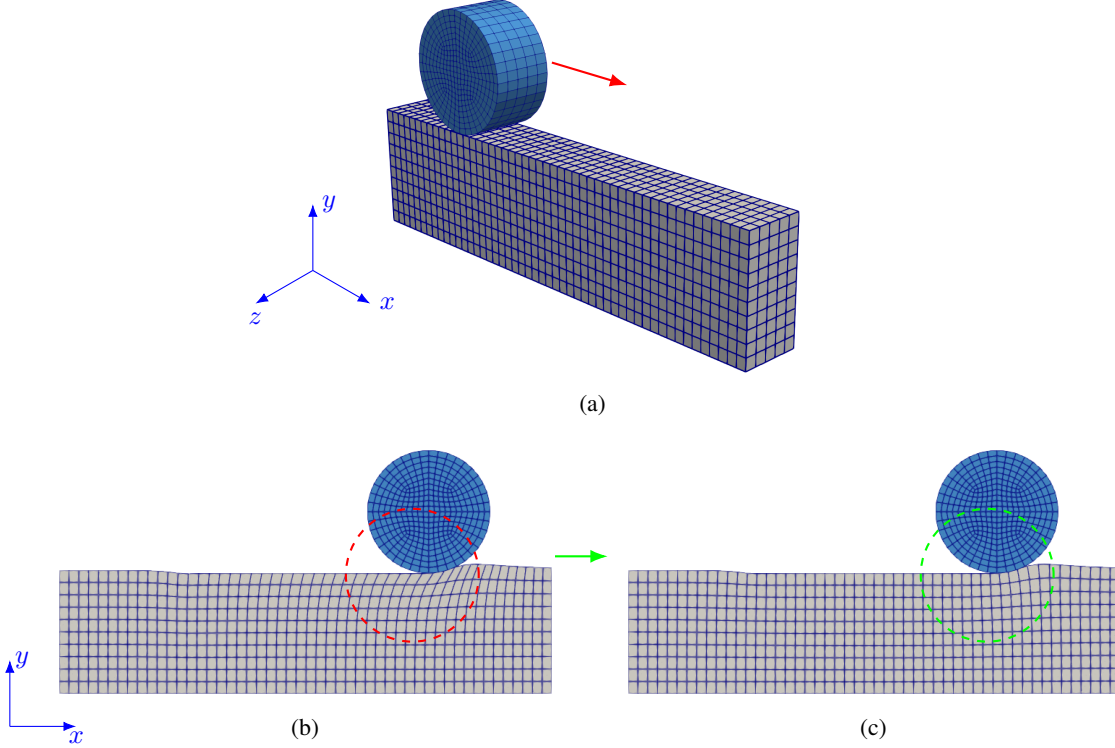


Figure 5: Frictional sliding of a rigid cylinder with a diameter of 0.25 over a rectangular block of dimensions $1 \times 0.25 \times 0.125$: (a) initial configuration. (b) the deformed state without mesh refitting (c) relaxed mesh for the deformed state in (b).

The second example investigates the punching of a rectangular block by a rigid hollow sphere. Only a quarter part is modeled because of the symmetry (see Figure 6a). The quarter rectangular block of size $0.5 \times 0.5 \times 0.25$ is modeled with an elasto-plastic constitutive model [42] and meshed with 13500 cubic 8-noded hexahedral elements. The rigid quarter sphere has an outer radius of 0.25 and is represented by the blue colored body in Figure 6a. Isothermal frictionless contact is applied as presented in Section 2.3. The sphere segment is moved vertically downwards through a distance equal to half of the block thickness, i.e., 0.125. This induces plastic deformations in the rectangular block as depicted in Figures 6b and 6d. The elements near the boundary are largely distorted, especially in the transition region between the contact and non-contact areas (highlighted by the red dashed circle in Figure 6d). The refitted mesh for this problem is depicted in Figures 6c and 6e. For the mesh refitting problem, the reference state update procedure is not performed ($\mathbf{X}_{\Omega_m} = \mathbf{x}_{\Omega_m}^{n+1}$), only the boundary displacement is transferred from the elasto-plastic problem. The refitted mesh contains less distorted elements at the boundary and inside the volume. Furthermore, the contact area has more elements than the original problem. Also, the quality of elements in the transition zone between the contact and the non-contact area (green dashed circle in Figure 6e) is improved. In conclusion, the mesh sliding method enables the movement of boundary elements or nodes to the region of interest and is thereby increasing the mesh quality at these regions. It also enables a smooth transition from the boundary to the volume mesh. Furthermore, mesh sliding is required to obtain the proper mesh relaxation for problems with large boundary distortion.

3.1.4 Algorithmic aspects of the mesh refitting method

In the following, more detailed algorithmic aspects of the overall mesh refitting approach will be presented.

Target shape incrementation scheme

The non-linear problem in (42) may not be solvable in one step if the old mesh is heavily distorted. To improve convergence of the Newton-Raphson scheme we employ an incrementation approach to the target lengths in (37) and target angles in (39). Thereto, we define N incrementation steps for the mesh refitting algorithm during which the incrementation factor $\alpha_{n_{inc}} \in [0, 1]$, with $n_{inc} \in 1, \dots, N$, is increased from 0 to 1. Let l_{e0}^i and θ_{e0}^{ij} be the element average lengths and angles of the original distorted mesh at the beginning of the algorithm (updated reference

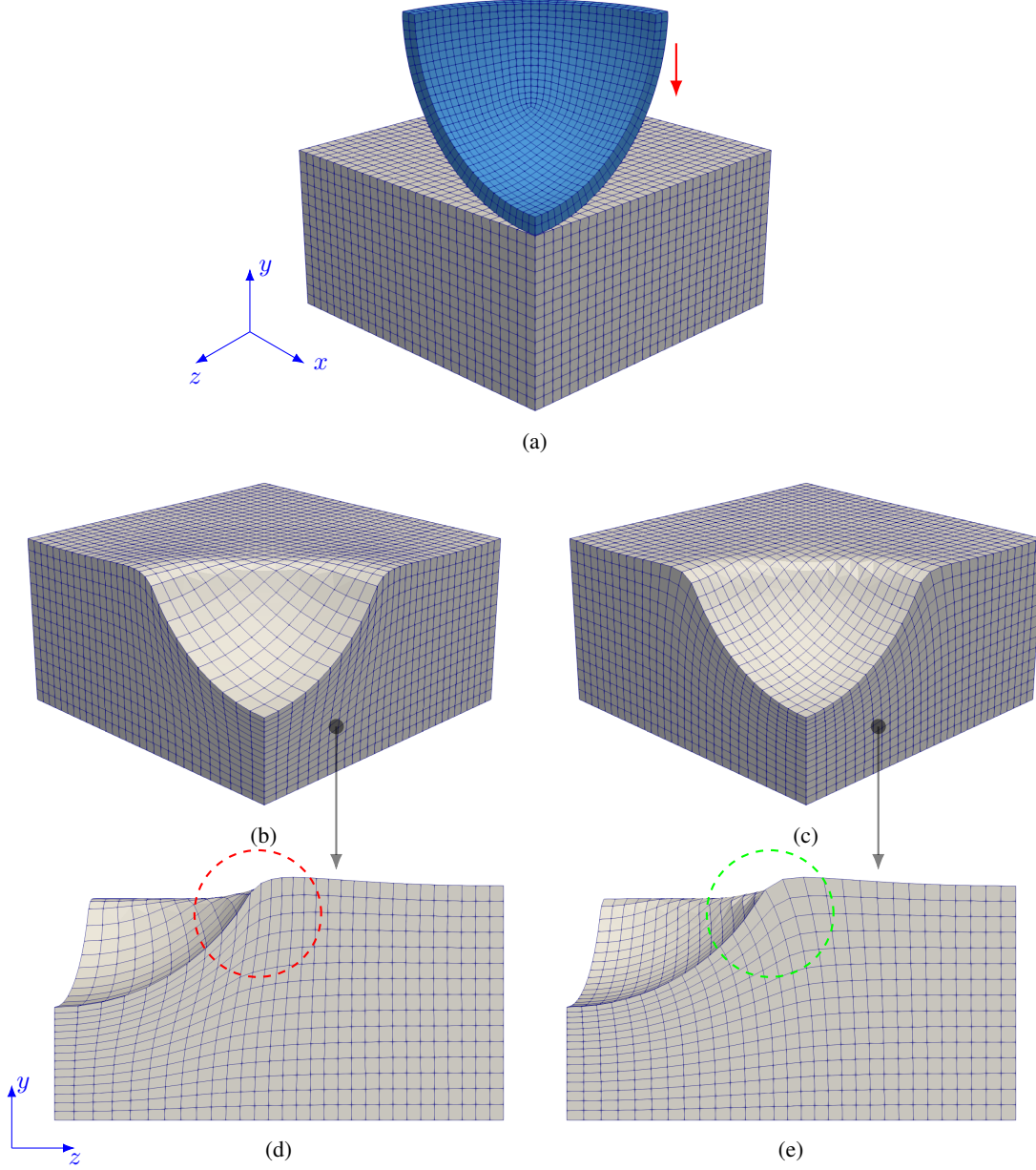


Figure 6: Elasto-plastic punching of a rectangular block of dimensions $0.5 \times 0.5 \times 0.25$ by a rigid hollow sphere of outer radius 0.25: (a) reference configuration. (b) final deformed state and (d) corresponding side view. (c) The solution of a parallel mesh refitting problem and (e) corresponding side view.

configuration). Moreover, l_r^i and θ_r^{ij} are the target element edge lengths and angles to achieve. Then, for the current incrementation step n_{inc} , the element reference lengths and angles are defined as

$$(l_r^i)_{n_{inc}} = l_{e0}^i + \alpha_{n_{inc}} (l_r^i - l_{e0}^i), \quad (43)$$

$$(\theta_r^{ij})_{n_{inc}} = \theta_{e0}^{ij} + \alpha_{n_{inc}} (\theta_r^{ij} - \theta_{e0}^{ij}). \quad (44)$$

Within this work for the numerical examples, the target angles are set to $\pi/2$, i.e., $\theta_r^{ij} = \pi/4$.

Remark 3.1.3. *The target incrementation scheme is similar to the classical substepping procedure. When a Newton step is not converged the step is subdivided. Furthermore, when a substep is not converged, the substep is further subdivided. However, when consecutive sub-steps are converged the sub-step size can be increased.*

Uniform mesh regularization

The aim of a purely uniform mesh regularization is to achieve uniform element sizes and shapes inside the entire problem domain. To achieve this goal, we prescribe the target element edge lengths as the average element edge length within the total problem domain determined for the (original) distorted mesh. The average edge length \bar{l}_r^i is defined as

$$\bar{l}_r^i = \frac{1}{N_e} \sum_j^{N_e} \|(\bar{\mathbf{v}}^i)_j\|, \quad (45)$$

where N_e is the number of elements in Ω_m and the index i refers to the direction e^i in parameter space.

Mesh localization

To achieve different target element edge lengths at different locations of the problem domain, we define a continuous spatial distribution function for l_r^i :

$$l_r^i(\mathbf{X}) = l_{r0}^i f(\mathbf{X}), \quad (46)$$

where $f(\mathbf{X})$ is a spatial function and l_{r0}^i is a reference value of the target element edge length. In this work, we employ the following exponential function:

$$f(\mathbf{X}) = \exp(-c \|\mathbf{X} - \mathbf{X}_0\|^2), \quad (47)$$

where the parameter c controls the rate of decay of the function when departing from the reference point \mathbf{X}_0 . According to (47), the distribution function $l_r^i(\mathbf{X})$ reproduces the reference value l_{r0}^i when evaluated at the reference point \mathbf{X}_0 . In practice, the reference point \mathbf{X}_0 typically represents a location of the physical problem, which is characterized by strong gradients of the primary variables accompanied by a significant mesh distortion. Thus, the mesh localization approach allows to have smaller elements, i.e., a higher mesh resolution, at this location. Moreover, to enforce a high mesh quality, i.e., small element distortions, at this critical location, also the penalty parameters may be prescribed as spatial functions based on (47), i.e., $\varepsilon_E(\mathbf{X}) = \varepsilon_{E0} f(\mathbf{X})$ and $\varepsilon_A(\mathbf{X}) = \varepsilon_{A0} f(\mathbf{X})$.

Demonstration example: Uniform mesh regularization and localization

Uniform mesh regularization and localization shall be illustrated by a 2-dimensional numerical example defined on a 2×2 domain. The initial distorted mesh is created by 40 unequal divisions of the edges resulting in 1600 elements as illustrated in Figure 7a. To achieve a uniform regularized mesh, we set the reference lengths to an average length according to (45). The resulting mesh is shown in Figure 7b, which clearly confirms the underlying idea of the uniform mesh regularization approach. Moreover, a localization is achieved using an exponential function according to (47) with $l_{r0}^i = 0.025$, $c = 0.1$, and \mathbf{X}_0 representing the center of the domain. The resulting mesh is portrayed in Figure 7c. As desired, this approach allows to achieve a higher mesh resolution with very regular elements at the location of interest, i.e., the center of the domain. Of course this ansatz compromises the mesh quality in other regions of the problem setup. Nevertheless, it can be very helpful in scenarios with very strict requirements on the mesh quality in certain regions of the problem.

3.2 Transfer of mesh data

Within our overall mesh refitting approach, the transfer of data from the old (distorted) mesh on Ω_m to the new (regularized) mesh on Ω'_m is a critical aspect. The variables to be transferred include nodal primary variables (i.e., displacement and temperature field) but also internal material variables (e.g., the inelastic deformation gradient) defined at quadrature points. These variables can be broadly classified as scalars, vectors, and tensors, whereas the latter represents the most challenging case from a data transfer point of view. This section presents the main strategy for data transfer as employed in this work including a tensor interpolation scheme proposed in our recent contribution [22]. It is emphasized that the proposed data transfer schemes are independent of the mesh refitting scheme proposed in the previous sections, and can be combined with arbitrary mesh regularization, mesh refinement and remeshing schemes.

Consider an element node or quadrature point located at \mathbf{x}_p in the new mesh Ω'_m . To determine the new data at \mathbf{x}_p , we interpolate data from an element patch $\Omega_p \subset \Omega_m$ within a radius of r_p around this point (see Figure 8). Let $\mathbf{x}_j \in \{\mathbf{x}_1, \dots, \mathbf{x}_N\}$ be a set of position vectors in Ω_p , while $\alpha_j \in \{\alpha_1, \dots, \alpha_N\}$ and $\mathbf{T}_j \in \{\mathbf{T}_1, \dots, \mathbf{T}_N\}$ represent scalar- and tensor-valued data associated with these points. The methods presented in the following rely on a relative weighting of data considering the distance of the data points from the interpolation point. For this purpose, we employ

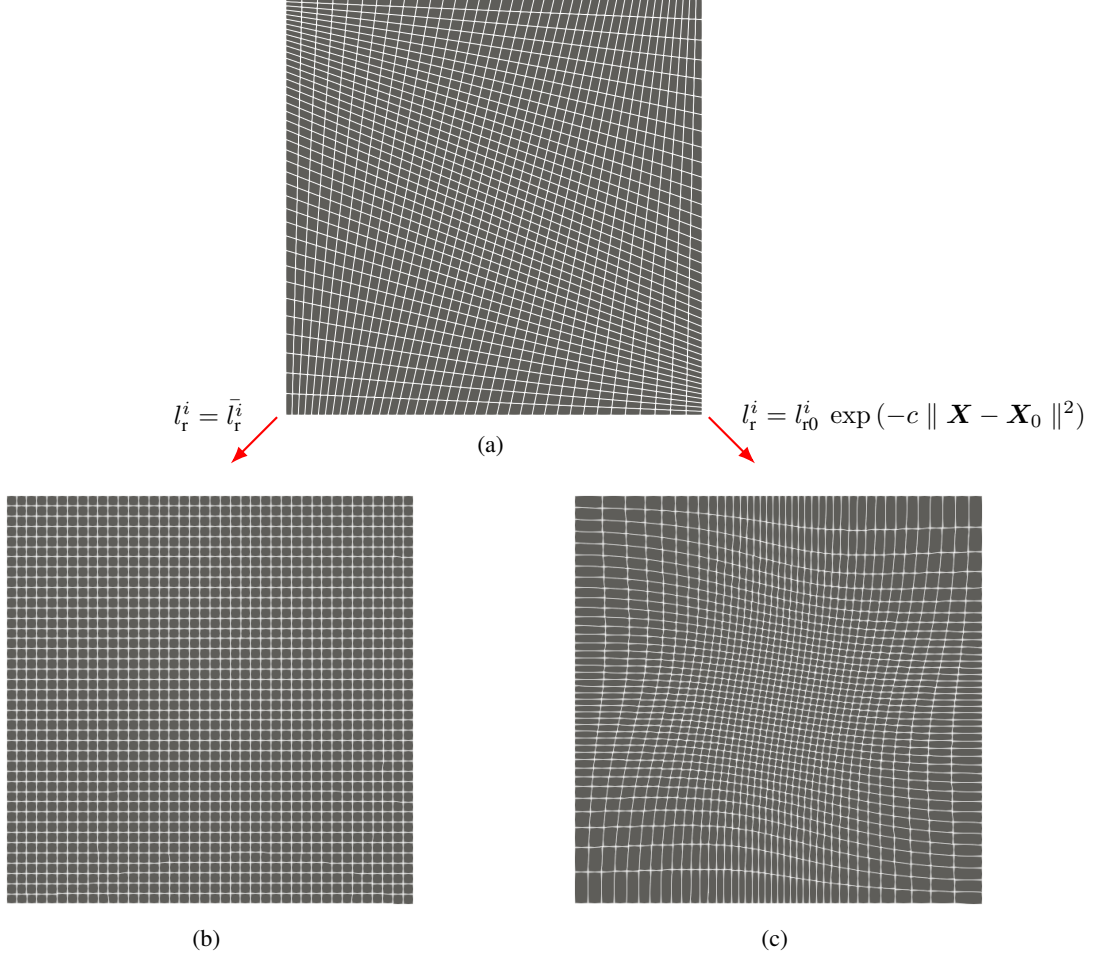


Figure 7: Illustration of mesh regularization and localization: (a) initial distorted mesh (b) regularized mesh (c) localized mesh with smaller elements at center of the square.

the normalized weighting function $\tilde{w}(\mathbf{x}_j)$ according to:

$$\tilde{w}(\mathbf{x}_j) := \frac{w(\mathbf{x}_j)}{\sum_{j=1}^N w(\mathbf{x}_j)} \quad \text{such that} \quad \sum_j \tilde{w}(\mathbf{x}_j) = 1. \quad (48)$$

Here the weighting function $w(\mathbf{x}_j)$ can be any monotonic continuous function that decreases as it moves away from the interpolation point \mathbf{x}_p . For example, an exponential weighting function with control parameter c reads:

$$w(\mathbf{x}_j) = \exp(-c \|\mathbf{x}_j - \mathbf{x}_p\|^2). \quad (49)$$

In the following subsection, we demonstrate methods to compute scalars and tensors at \mathbf{x}_p , denoted as α_p and \mathbf{T}_p .

3.2.1 Scalar interpolation

We employ two different schemes for scalar interpolation, namely the moving least squares (MLS) and the logarithmic moving least squares (LOGMLS) method. Importantly, the LOGMLS scheme preserves strict positivity of strictly positive data ($\alpha_j > 0$), but, in turn, is limited to data exhibiting this property. Furthermore, both methods preserve important additional properties such as monotonicity of the data. The two schemes are briefly outlined below.

1. *Moving least squares (MLS)*: This variant employs a spatial polynomial approximation which reads

$$\alpha(\mathbf{x}) := \mathbf{p}(\mathbf{x})\mathbf{a}, \quad (50)$$

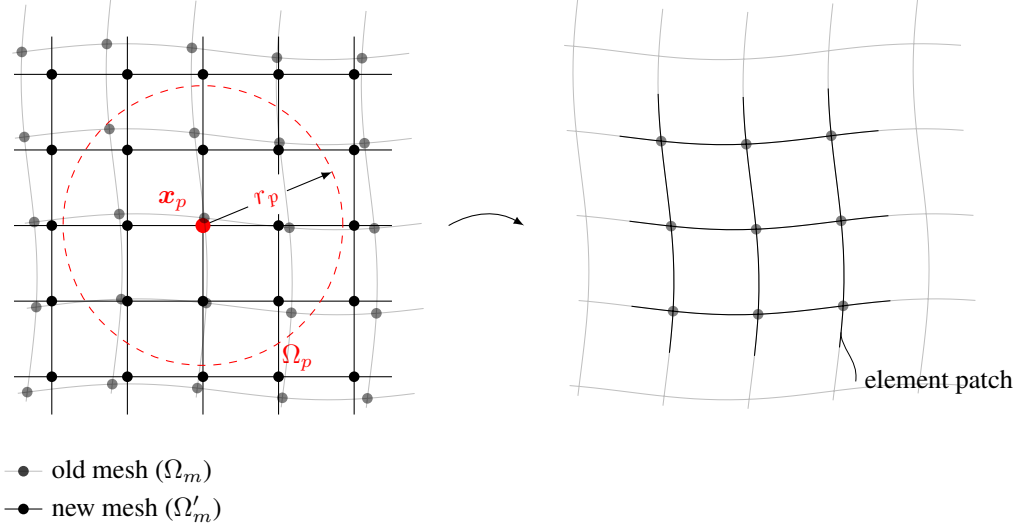


Figure 8: Illustration of element patch for transferring data from old mesh to new mesh.

where $\mathbf{p}(\mathbf{x}) \in \mathbb{R}^m$ is the vector of polynomial basis functions of order m , and $\mathbf{a} \in \mathbb{R}^m$ is the corresponding vector of coefficients. The unknown coefficient vector \mathbf{a} is obtained by minimizing the residual

$$r = \sum_{j=1}^N \tilde{w}(\mathbf{x}_j) (\mathbf{p}(\mathbf{x}_j) \mathbf{a} - \alpha_j)^2. \quad (51)$$

As a prerequisite, the order of the polynomial function m must be chosen such that $m \leq N$.

2. *Logarithmic moving least squares (LOGMLS)*): This method ensures non-negative interpolation of positive quantities. It employs a moving least squares approximation of a logarithmically transformed scalar field:

$$\alpha(\mathbf{x}) := \exp(\mathbf{p}(\mathbf{x}) \mathbf{a}). \quad (52)$$

In this approach, the unknown vector of coefficients \mathbf{a} is found by minimizing the residual

$$r = \sum_{j=1}^N \tilde{w}(\mathbf{x}_j) (\mathbf{p}(\mathbf{x}_j) \mathbf{a} - \ln(\alpha_j))^2. \quad (53)$$

For a detailed analysis of these two methods the reader may refer to our previous work [22].

3.2.2 Tensor interpolation

We employ rotation vector-based methods for tensor interpolation proposed in our previous work [22]. These methods exploit the polar and spectral decomposition of the tensor data according to $\mathbf{T}_j = \mathbf{R}_j \mathbf{Q}_j^T \mathbf{\Lambda}_j \mathbf{Q}_j$, where $\mathbf{R}_j, \mathbf{Q}_j \in \mathbb{SO}(3)$ are rotation tensors and $\mathbf{\Lambda}_j$ is the positive definite diagonal tensor containing the eigenvalues of \mathbf{T}_j . The general strategy for tensor interpolation relies on an individual interpolation of the rotation tensors and the eigenvalues contained in $\mathbf{\Lambda}_j$. First, the scalar eigenvalues are individually interpolated using the schemes from Section 3.2.1 to finally reconstruct $\mathbf{\Lambda}_p$. For interpolation of the rotation tensors $\mathbf{R}_j, \mathbf{Q}_j$ specific schemes are employed that preserve, among others, the objectivity of the underlying mechanical problem and are well-established in the field of geometrically exact beam theories [43]. This step results in the interpolated rotation tensors $\mathbf{R}_p, \mathbf{Q}_p$. Finally, the interpolated tensor \mathbf{T}_p at \mathbf{x}_p is reconstructed according to $\mathbf{T}_p = \mathbf{R}_p \mathbf{Q}_p^T \mathbf{\Lambda}_p \mathbf{Q}_p$.

These interpolation methods are well suited for any invertible second-order tensor. In the context of finite element discretizations for problems of nonlinear continuum mechanics, tensor-valued history often arises for material models involving, e.g., inelastic constitutive behavior [44, 45, 46] or phase change [47, 48, 49]. Generally, these methods have been proven to preserve important properties of the tensor during interpolation (e.g., positive definiteness, objectivity, etc.) and allow for higher-order spatial convergence.

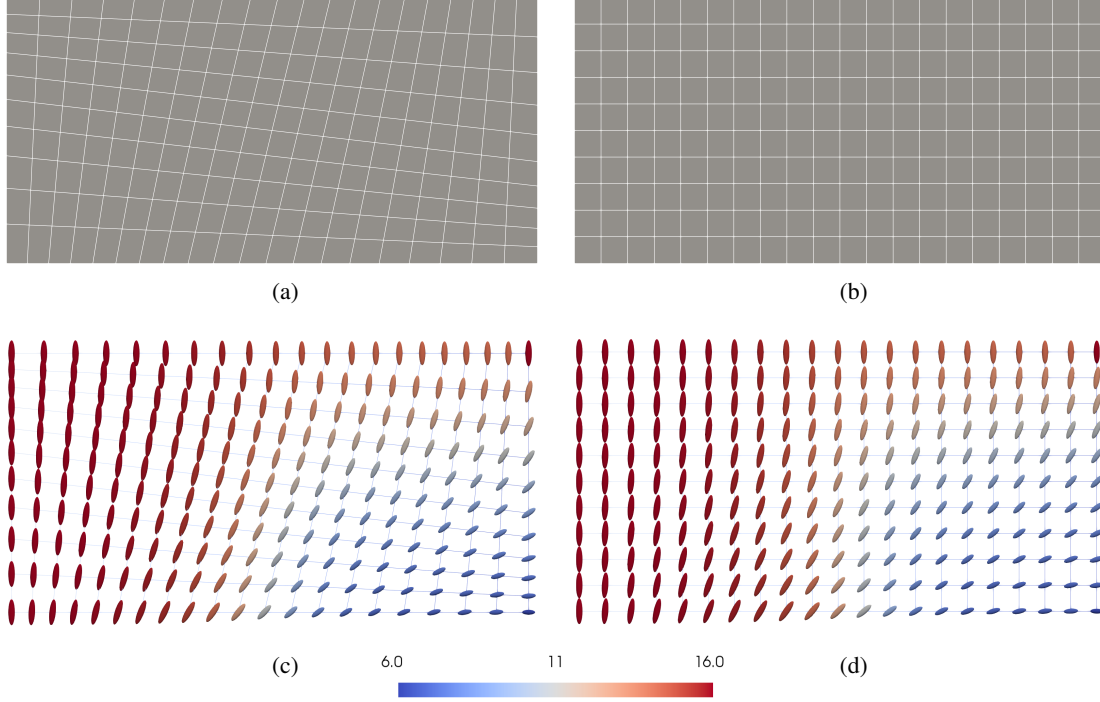


Figure 9: Tensor interpolation example: (a) input mesh (b) regularized mesh (c) ellipsoidal representation of input tensor field (d) ellipsoidal representation of mapped tensor field. The color represents the determinant of the tensor.

Demonstration example: Transfer of tensor data

The tensor interpolation as part of the mesh adaptation approach is portrayed in Figure 9. Consider an initial mesh as visualized in Figure 9a with a tensor field as illustrated in Figure 9c (ellipsoidal representation, see [22]). Now, the mesh regularization is performed as described in Section 3.1.3 and the resulting mesh is shown in Figure 9b. For tensor interpolation, we employed the "R-MLS" variant as defined in our previous work [22] to transfer tensor data from the old to the new mesh. From Figures 9c and 9d it is evident that the method delivers a smooth interpolation while preserving the magnitude and orientation of the tensor data when mapped.

4 Numerical results

In this section we show the capabilities of the proposed mesh adaptation scheme using different numerical examples.

4.1 Expansion past a rigid obstruction

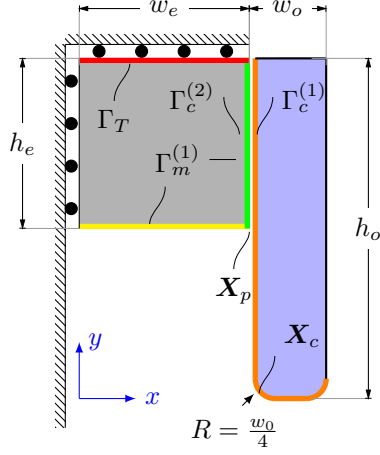
Table 1: Material parameters of the expanding material

Parameter	Value
Young's modulus (E)	1×10^4
Poisson's ratio (ν)	0
thermal conductivity (k_0)	7.55×10^6
Heat capacity (c_v)	1.4×10^{-2}

Table 2: Mesh refitting parameters

Parameter	Value
$\bar{\epsilon}_E, \hat{\epsilon}_E, \epsilon_A$	1×10^{-2}
ϵ_m	2×10^8
Maximum n_{inc}	20
Displacement tolerance	1×10^{-5}

As the first numerical example, we explore a pseudo 2-dimensional expansion past a rigid body as illustrated in Figure 10. The geometry and the boundary conditions are depicted in Figure 10a and the corresponding dimensions are given in Figure 10b. The expanding material is modeled as presented in Section 2.2, with $\alpha = 0$ allowing an unlimited expansion. It's elastic behavior described by Ψ_e is modeled using a Neo-Hookean material model with parameters



Quantity	Value
height h_e	1
width w_e	1
thickness t_e	0.1
height h_o	2
width w_o	1/4
thickness t_o	0.1

(a)

(b)

Figure 10: Example 1: Problem setup with a grey body denoting the expanding material and a violet body representing the obstruction. (a) geometry and boundary conditions (b) dimensions.

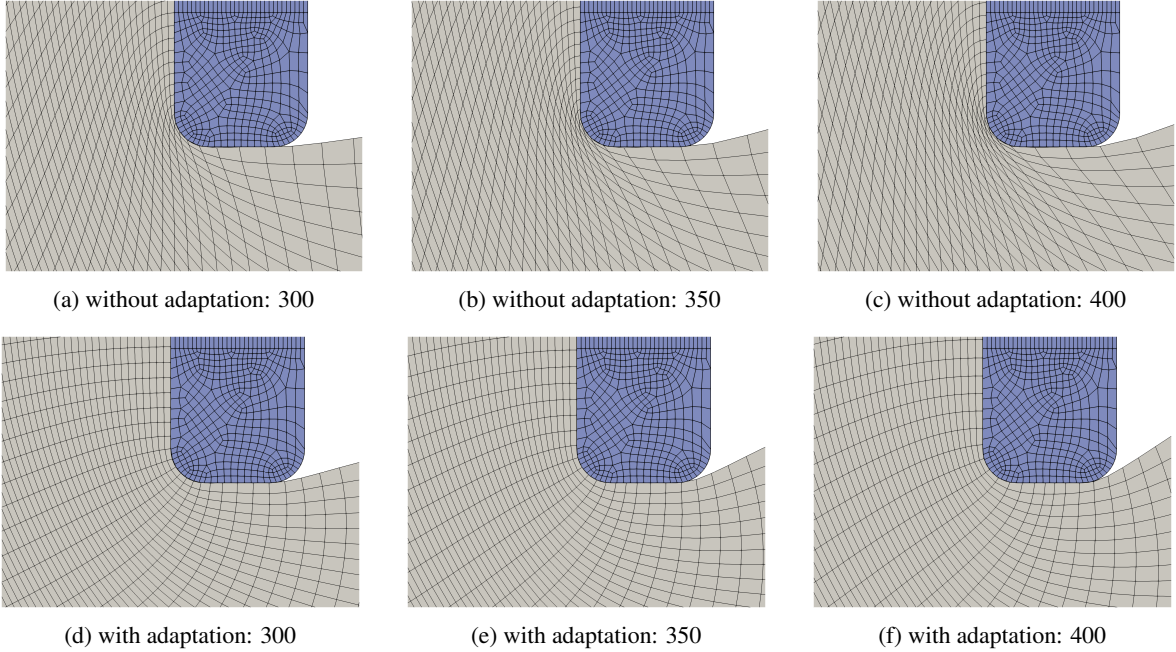
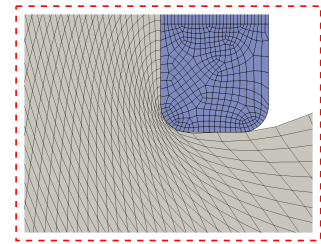
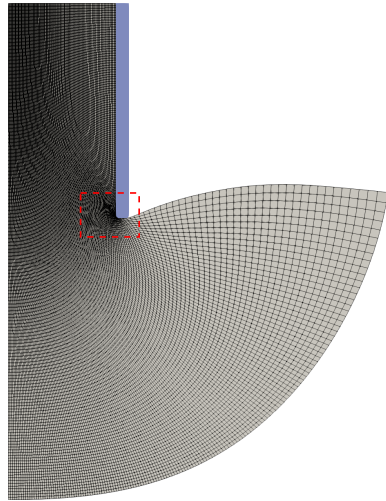
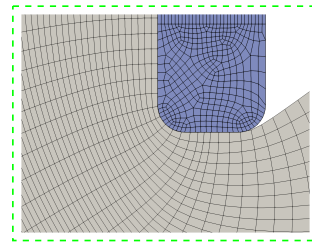
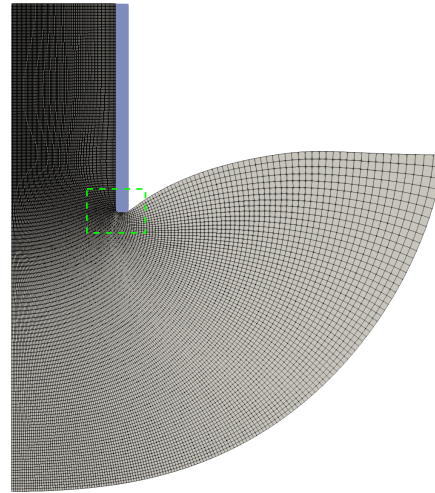


Figure 11: Example 1: Mesh around the corner (a)-(c) without mesh adaptation and (d)-(f) with mesh adaptation for time steps 300, 350, and 400, respectively

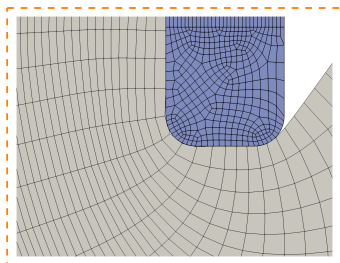
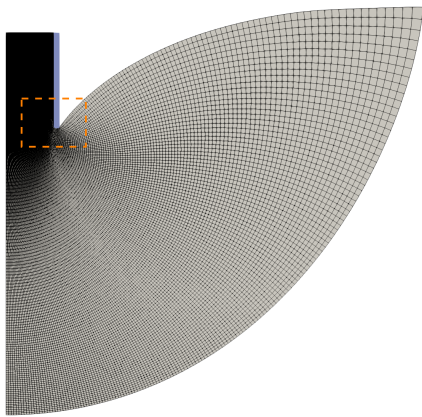
listed in Table 1. The expansion is restricted to $+x$ and $-y$ direction by arresting the normal displacements as shown in Figure 10a. Furthermore, the initial temperature T_0 is set to 148 and a temperature surface Dirichlet boundary condition $T = T_0 + 345 \log_{10}(1 + [(8 \times (t + 3))/60])$ is applied to Γ_T . Finally, to avoid 3-dimensional effects, the displacements in z -direction are arrested. Both, the expanding and the rigid body are discretized with \mathbb{Q}_1 8-noded hexahedral elements with 22500 (45602 nodes) and 6414 elements (13092 nodes) with one element in the thickness direction, respectively. For the mortar thermo-mechanical contact, the outer surface of the rigid body is chosen as the slave side and the surface of the expanding material as the master side. The contact interface is discretized with 4-noded quadrilateral elements, where the contact penalty parameter is set to $\epsilon_c = 1 \times 10^8$ and the interface conductivity to $\beta_c = 0$, i.e., modeling adiabatic contact. The linearized monolithic thermomechanical system is solved using the iterative GMRES method with AMG(BGS) preconditioner. The convergence tolerance on the combined residual and increment is set to 10^{-8} . The thermo-mechanical problem is analyzed for 1000 steps using a time step size $\Delta t = 0.05$.



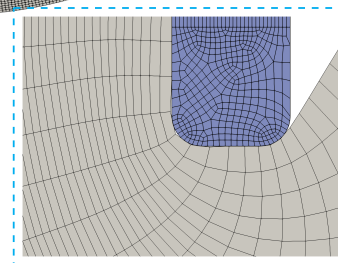
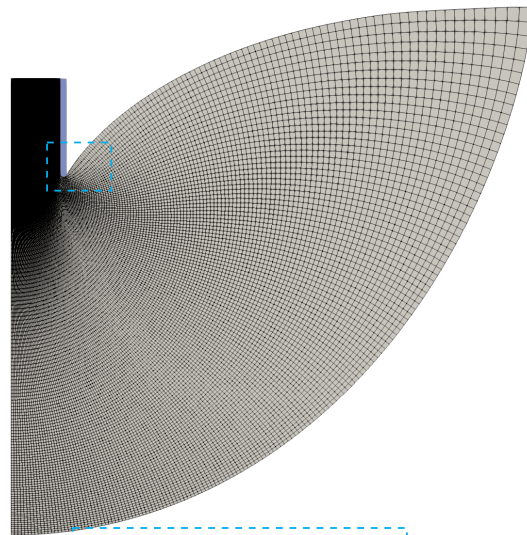
(a) without adaptation: step 425



(b) with adaptation: step 425



(c) step 800



(d) step 1000

Figure 12: Example 1: deformed state at step (a) 800 and (b) 1000 with adaptation.

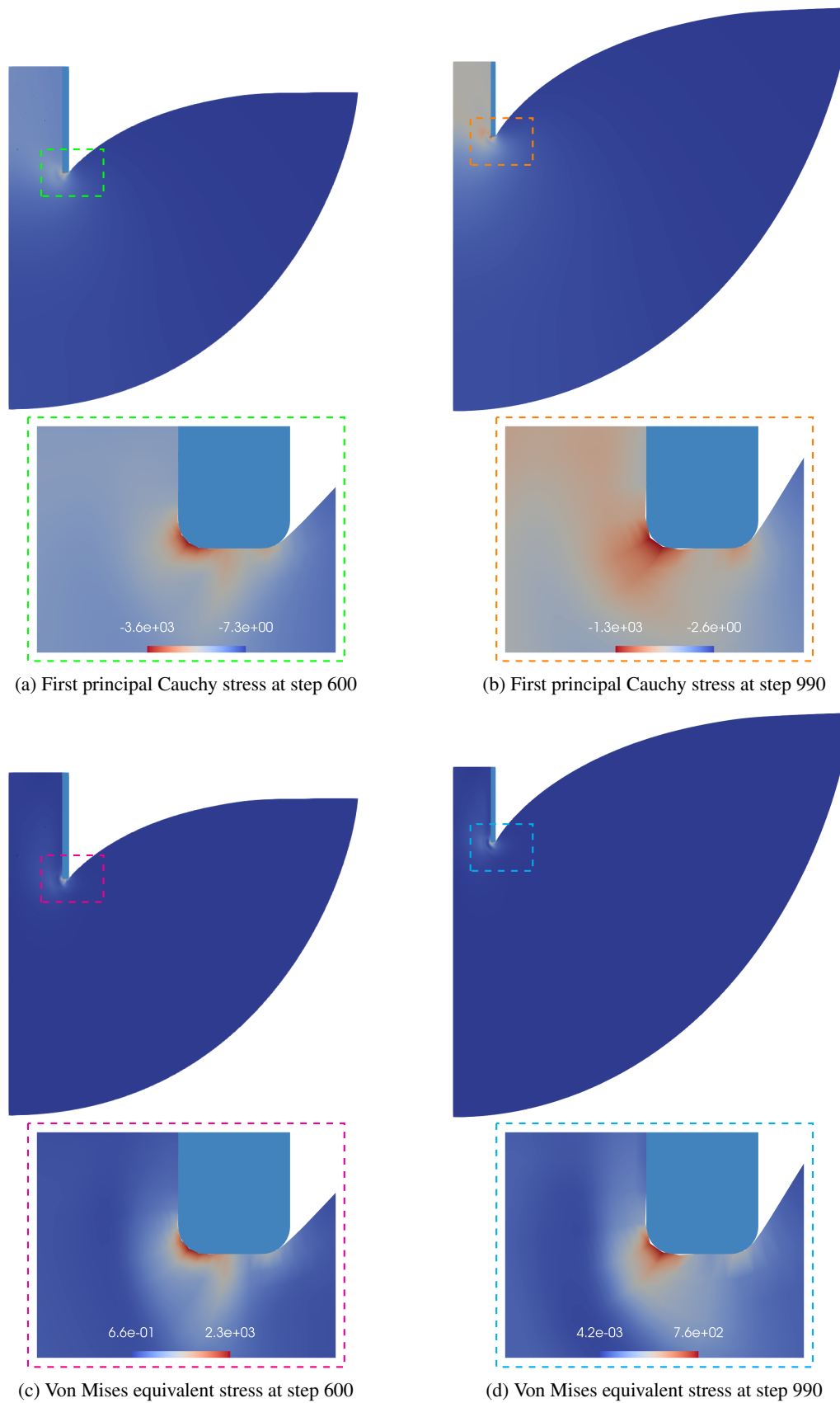


Figure 13: Example 1: Von Mises equivalent stress and first principal Cauchy stress (maximum compressive) at steps 600 and 990.

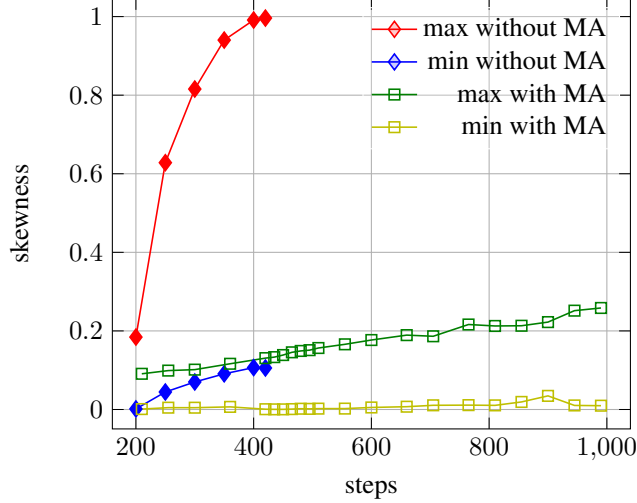


Figure 14: Example 1: Comparison of minimum and maximum skewness (SK) over time steps in the corner region around \mathbf{X}_c with radius $r = 0.1$ for the problem with and without mesh adaptation (MA).

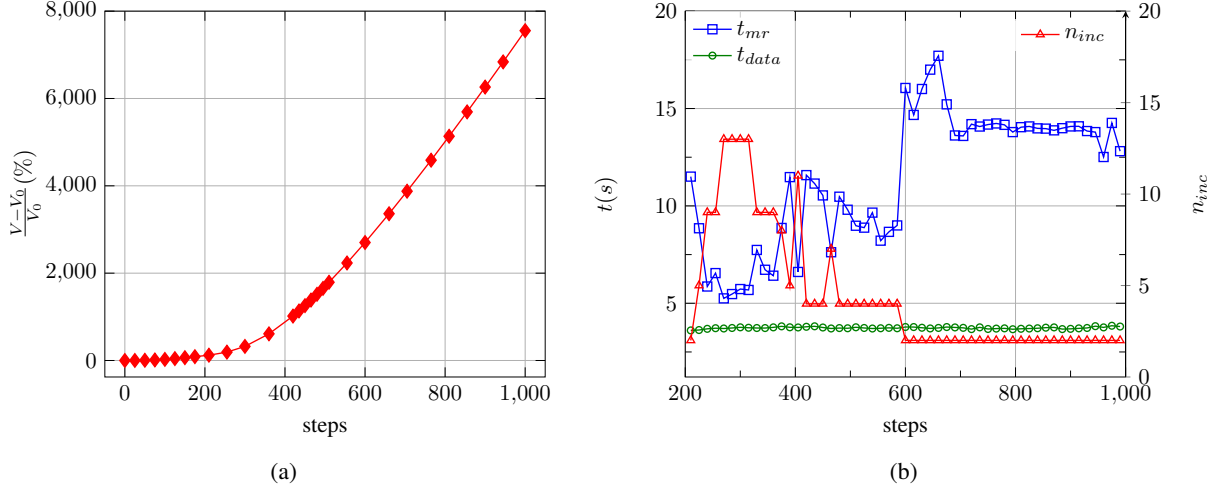


Figure 15: Example 1: (a) percentage increase in total volume ($\frac{V-V_0}{V_0}$) vs. step. (b) computation time viz, time for mesh refitting step t_{mr} per incrementation steps n_{inc} and data mapping t_{data} time for each mesh adaptation step.

The accompanying mesh adaptation problem is formulated as follows: to achieve a good quality mesh around the corner \mathbf{X}_c (see Figure 10a), we employ a mesh localization as in (46) and (47) with $c = 100$. The reference lengths in each time step are estimated as in (45) and mesh refitting parameters as listed in Table 2. The mesh sliding surfaces $\Gamma_m^{(1)}$ in reference configuration are portrayed in the Figure 10a. Furthermore, a Dirichlet boundary condition is applied to the corner node \mathbf{X}_P to minimize any potential topology change. The convergence tolerance for the residual and the displacement increment is set to 10^{-5} . Moreover, the linearized system is solved with the "SuperLU" direct solver. For the material model as presented in Section 2.2, the computation of the inelastic deformation gradient \mathbf{F}_{in}^{m+1} requires \mathbf{F}_{in}^n , \mathbf{F}^n , \mathbf{S}^n , and T^n . As a result, this data has to be transferred from the old mesh to the new mesh. The tensor data \mathbf{F}_{in}^n is transferred from old mesh to new mesh by the "R-MLS" method with quadratic basis (see Section 3.2.2), the deformation gradient \mathbf{F}^n is reconstructed from nodal displacements, and the stress \mathbf{S}^n and temperature T^n are interpolated as scalar using moving least square with quadratic basis (see Section 3.2.1). The mesh adaptation is carried out every 15th step starting from step 210. Finally, the computation is carried out on 2 nodes (48 CPUs) of an Intel Xeon E5-2680v3 2.5GHz processor.

First, the results without adaption are investigated. As expected, once the expanded material passes the corner, the mesh quality reduces (see Figures 11a to 11c). The element skewness around the corner \mathbf{X}_c in the radius 0.1 is plotted over

the time in Figure 14. It can be seen that the skewness increases rapidly, starting from time step 200 to 425. After step 250, the maximum skewness is greater than 0.6, which may affect the accuracy of the solution. At time step 425 (see Figure 12a), the elements are heavily distorted (skewness ≈ 1) such that computation can no longer be continued. However, a volume increase of about 863% is achieved at this step.

Next, the results including the proposed mesh adaptation scheme are studied. The mesh around the corner is portrayed in Figures 11d to 11f and 12b. Compared to the results without mesh adaptation, a mesh of higher quality is maintained around the corner (X_c) during the expansion. The skewness near the corner is greatly reduced throughout the simulation (see Figure 14). A slight increase in skewness can be attributed to the extreme volume expansion and shape change which can not be completely avoided. Figure 12b shows the expanded state at step 425, which has superior mesh quality compared to the simulation without mesh adaptation (see Figure 12a). Moreover, further states at steps 800 and 1000, that could only be produced/reached when the mesh adaptation is activated, are portrayed in Figures 12c and 12d. At the end of step 1000, there is a volume increase of approximately 7553%. The increase in volume over time steps is depicted in Figure 15a. The expansion can even be further carried out, but the element's aspect ratio keeps increasing. Furthermore, the mesh quality at step 1000 with a volume expansion of 7553% still way better compared to without MA at step 425 with volume increase 863%.

The first principal Cauchy stress for the with MA at steps 600 and 990 are plotted in Figures 13a and 13b. The Cauchy stress is obtained from the interpolated second Piola-Kirchhoff stress tensor (see Section 2.2). As expected, the stress is high near the kink X_c . As a result, the Von Mises equivalent stress near the region is higher, as depicted in Figures 13c and 13d.

The computation time for the mesh adaptation is plotted in Figure 15b. The figure portrays the time for the mesh refitting t_{mr} per incrementation step n_{inc} and the data mapping time t_{data} for every mesh adaptation step. Furthermore, the total time for the mesh adaptation step can be computed as $t_{mr}n_{inc} + t_{data}$. Time t_{mr} is the total time spent for the MR including all the necessary setup. For $n_{inc} > 1$, also the time spent on the unconverged Newton-Raphson iterations is included. On average t_{mr} is 13s. The data transfer time t_{data} is 4s and approximately constant. In the initial phase, specifically between steps 200 to 400 (see Figure 15a) the number of incrementation steps range between 5 to 13. However, as we progress, the incrementation requirement decreases significantly. From steps 600 to 1000, only two steps are needed for each mesh adaption. Finally, the computational time incurred per mesh adaptation step for the problem is on average 56s. The total simulation time is 10,960s wherein the mesh adaptation accounts for a share of 27%.

4.2 Expansion past a rigid obstruction and a deformable body

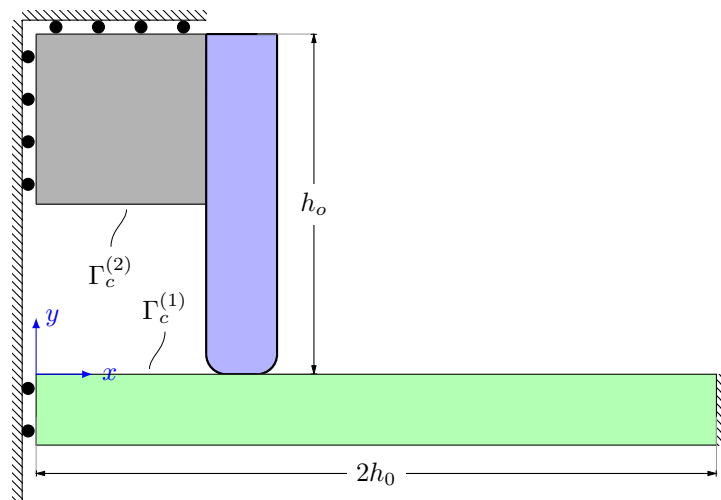
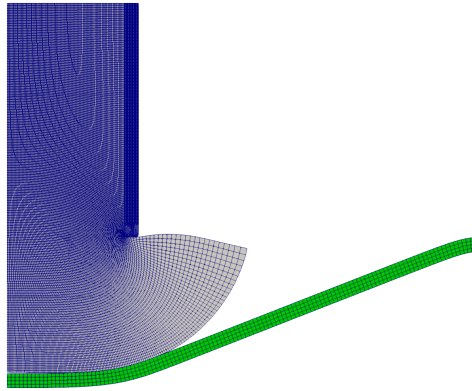
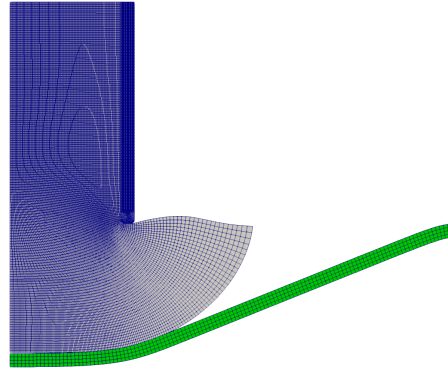


Figure 16: Example 2: Problem setup with a grey body denoting the material in expansion. The blue and green bodies represent the rigid body, and the deformable body, respectively.

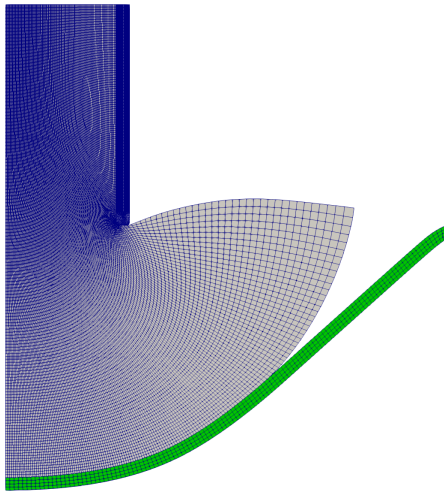
This example is an extension of the previous example, and the problem setup is illustrated in Figure 16. The dimensions, material properties, boundary conditions, and discretization of the expanding and rigid body are the same as in the previous example (see Figure 10, Table 1). The length of the deformable body (green) is twice the length of the rigid body, has the same thickness as the rigid body, and boundary conditions as illustrated in Figure 16. The deformable



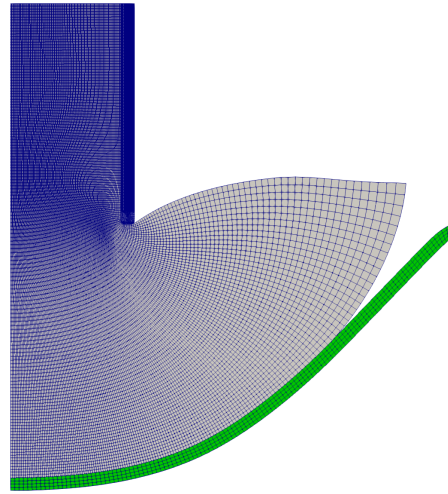
(a) without adaptation: 300



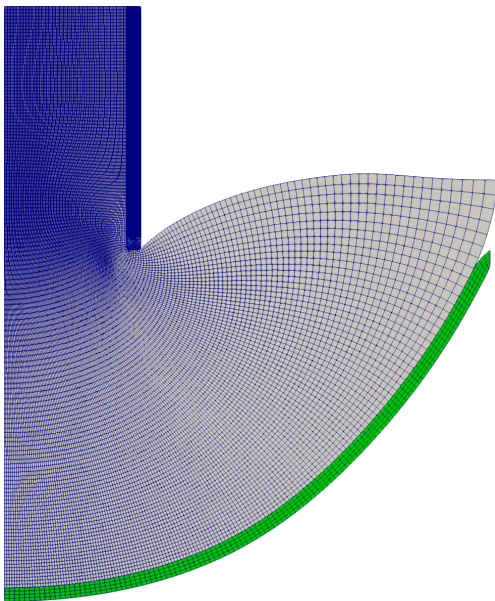
(b) with adaptation: 300



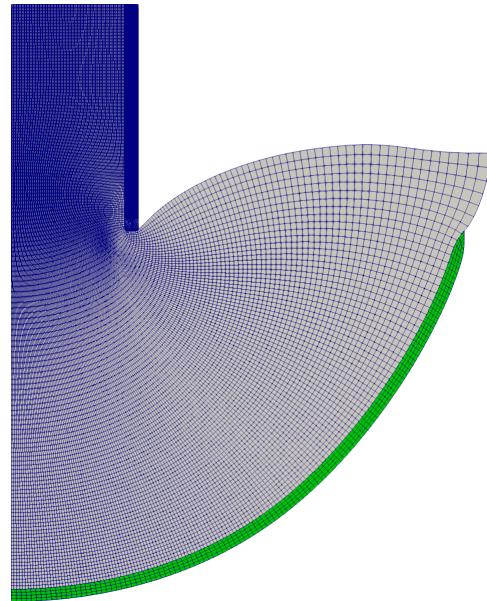
(c) without adaptation: 400



(d) with adaptation: 400



(e) with adaptation: 450



(f) with adaptation: 500

Figure 17: Example 2: (a) and (c) show the mesh without mesh adaptation at steps 300 and 400, respectively; (b) and (d) show the corresponding meshes with mesh adaptation. (e) and (f) mesh at steps 450 and 500 with mesh adaptation, respectively.

Table 3: Material properties of the deformable body

Parameter	Value
Young's modulus (E)	1×10^4
Poisson's ratio (ν)	0.3
thermal conductivity (k_0)	7.55×10^6
Heat capacity (c_v)	1.4×10^{-2}

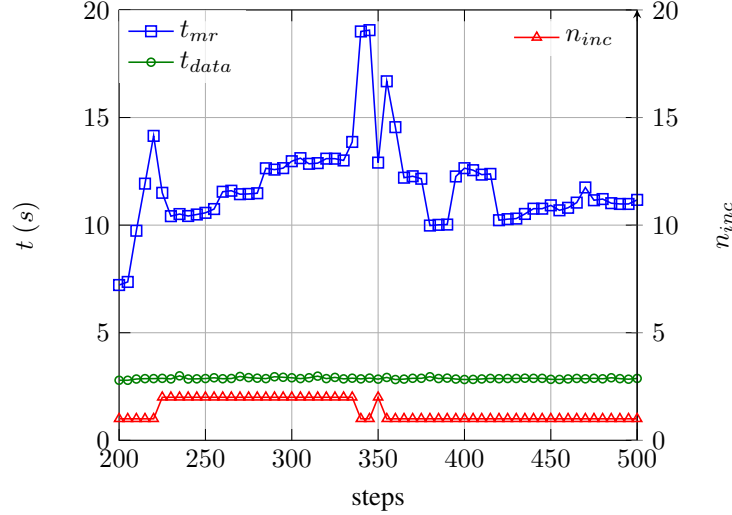


Figure 18: Example 2: Computation time viz, time for mesh refitting step t_{mr} per incrementation steps n_{inc} and data mapping t_{data} time for each mesh adaptation step.

body is modeled with Neo-Hookean material model with parameters as given in Table 3. For the thermomechanical mortar contact between the expanding and deformable body, the boundary of the first body is chosen as the master $\Gamma_c^{(2)}$ and the second as the slave side $\Gamma_c^{(1)}$ (see Figure 16). Furthermore, the penalty parameter for this contact pair is set to 1×10^7 , and the interface conductivity is $\beta_c = 0$, i.e., adiabatic contact. The deformable body is discretized with 420 linear hexahedral elements. Again, the linearized monolithic thermomechanical system is solved using the iterative GMRES method with AMG(BGS) preconditioner. The convergence tolerance on the combined residual and increment is set to 10^{-8} . The thermo-mechanical problem is analyzed for 500 steps with the time step size $\Delta t = 0.05$.

The mesh adaptation problem is formulated as follows: Like in the former example, to achieve good quality mesh around the corner \mathbf{X}_c , we employed a mesh localization as in (46) and (47) with $c = 100$. The reference lengths in a time step are estimated as in (45). The mesh refitting parameters are the same as the previous example and are listed in Table 2. Furthermore, a Dirichlet boundary condition is applied to the corner node \mathbf{X}_p such that any potential topology change can be minimized. The convergence tolerance for the residual and displacement increment is chosen to 10^{-5} and the linearized system is solved with the "SuperLU" solver. Again, the data transfer parameters remain the same as in the previous example. The mesh adaptation is carried out every 5th step starting from step 200. Finally, the computation is carried out on 3 nodes (72 CPUs) of an Intel Xeon E5-2680v3 2.5GHz processor.

The mesh during the expansion process is illustrated in Figure 17. The mesh for expansion without and with mesh adaptation for steps 300 and 400 are depicted in Figures 17a to 17d respectively. The mesh near the corner point \mathbf{X}_c (not plotted) shows the same trend as in the previous example (see Figure 11). The simulation without mesh adaptation fails at step 400 due to a heavily distorted mesh near \mathbf{X}_c . The deformed state with mesh adaptation at steps 450 and 500 are depicted in Figures 17e and 17f, respectively. Also in this example we get improved mesh quality compared to the scenario without MA, even for simulation times that are not accessible to simulations without MA.

The computational costs for the mesh adaptation procedure are presented in Figure 18. In contrast to the previous example, less incrementation steps (≤ 2) are necessary as the mesh adaption frequency is higher. The data transfer

time is $\leq 3s$ and t_{mr} is $15s$ on average. Finally, the average mesh adaptation computation time spent is $20s$. The total simulation time is $5,621s$ wherein the mesh adaptation accounts for a share of $\approx 20\%$.

4.3 Inward expansion of a hollow cylinder past a rigid obstruction

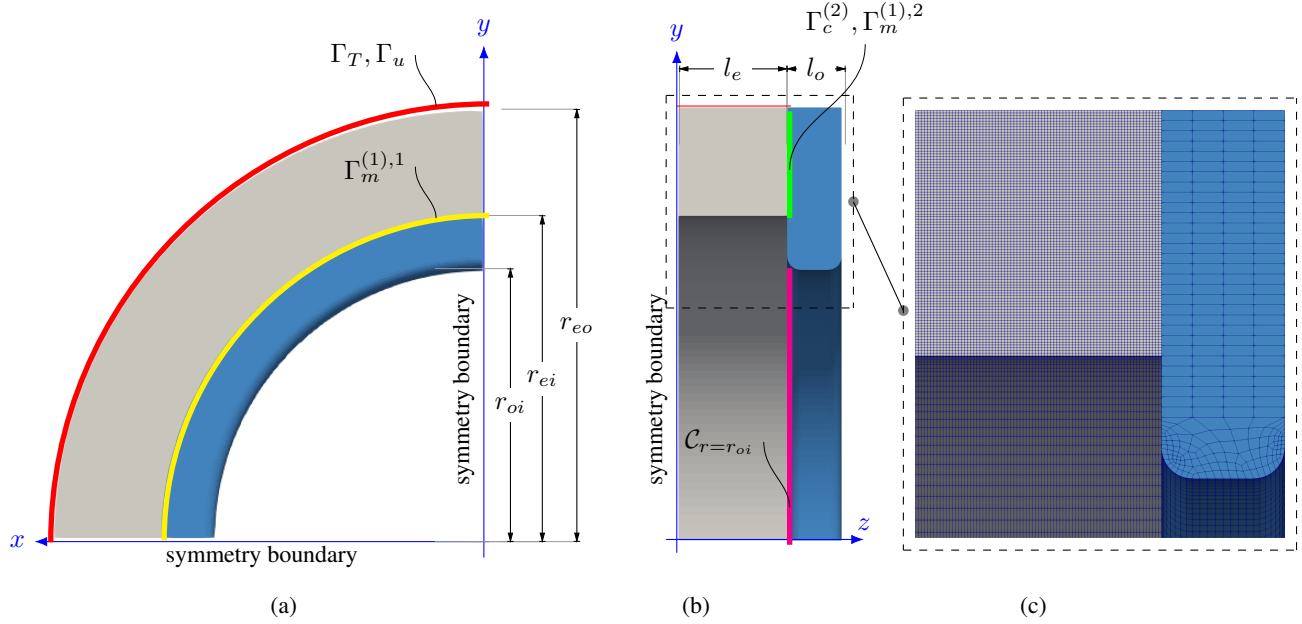


Figure 19: Example 3: expanding material (gray), obstruction (blue), and auxiliary boundary (green) (a) +z-plane view (b) +x-plane view (same as +y-plane due to symmetry). (c) mesh at reference configuration.

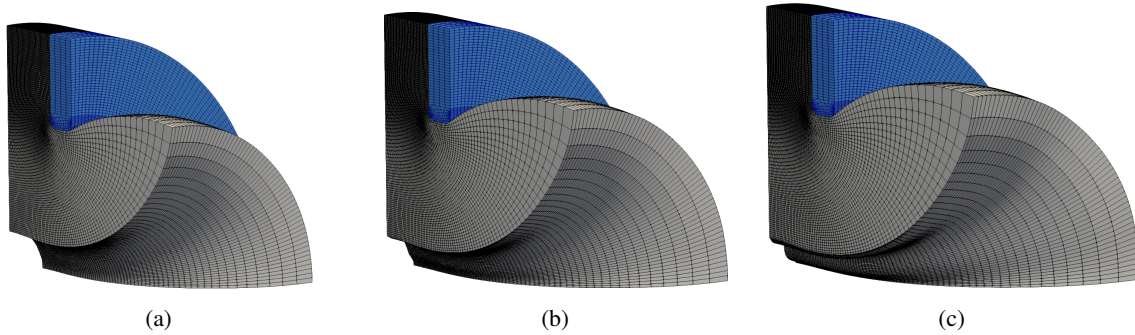


Figure 20.A: Example 3: deformed state at step (a) 360 (b) 400 (c) 428.

Next, the inward expansion of a hollow cylinder past a rigid obstruction is investigated. Consider the problem setup depicted in Figure 19. Due to symmetry, only a quarter portion of the system is simulated. The hollow quarter cylinder has an outer diameter $r_{eo} = 4$, inner diameter $r_{ei} = 3$, and length $l_e = 1$. The rigid body has the same outer diameter as the hollow cylinder's, the inner diameter $r_{oi} = 2.5$, and length $l_o = 0.5$. The corner radius of the rigid obstruction has the same relation as in Example 1 (see Figure 10). The material model of the expanding body is as described in Example 1 (Section 4.1). The initial temperature T_0 is set to 148 and a temperature surface Dirichlet boundary condition $T = T_0 + 345 \log_{10}(1 + [(8 \times (t + 3))/60])$ is applied at the outer surface of the expanding cylinder denoted by Γ_T . Apart from the symmetric structural boundaries (see Figure 19), the outer surface of expanding cylinder (denoted by Γ_u) is fixed. Both, the expanding and the rigid body are discretized with \mathbb{Q}_1 8-noded hexahedral elements with 432000 (449631 nodes) and 14700 elements (18178 nodes), respectively. For the mortar thermo-mechanical contact, the outer surface of the rigid body is chosen as the slave side and the surface of the expanding material as the master side ($\Gamma_c^{(2)}$). The contact interface is discretized with 4-noded quadrilateral elements, where the penalty parameter is set to $\epsilon_c = 10^8$ and interface conductivity $\beta_c = 0$, i.e., adiabatic. Again, the linearized monolithic thermomechanical system is solved

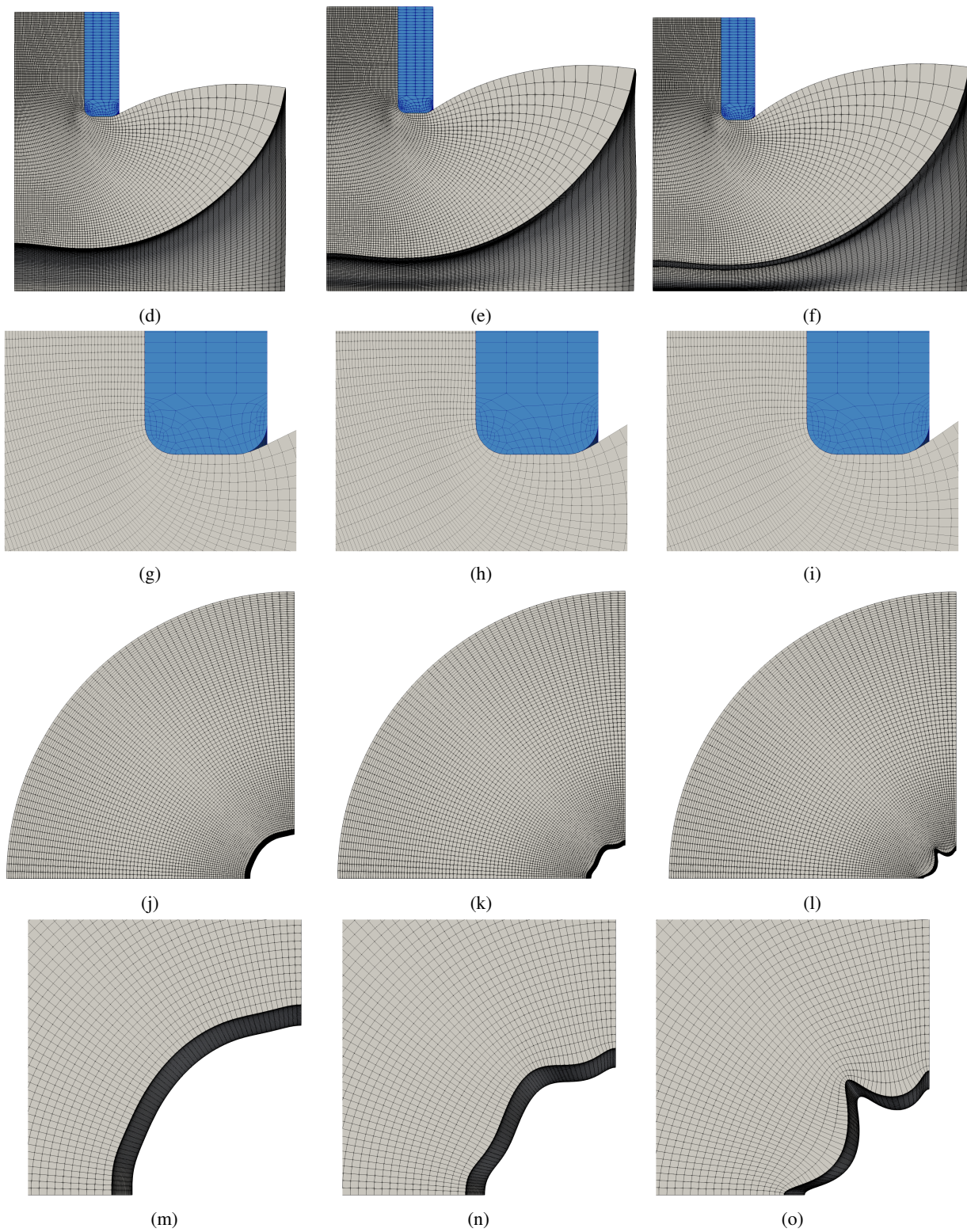


Figure 20.B: Example 3: deformed state at steps 360, 400, and 428 are illustrated in column 1, 2, and 3, respectively. Row 1: +x-plane view, Row 2: +x-plane detailed view around the fillet, Row 3: +z-plane view, and , Row 4: +z-plane view detailed view at the center (c.f. Figures 19a and 19b).

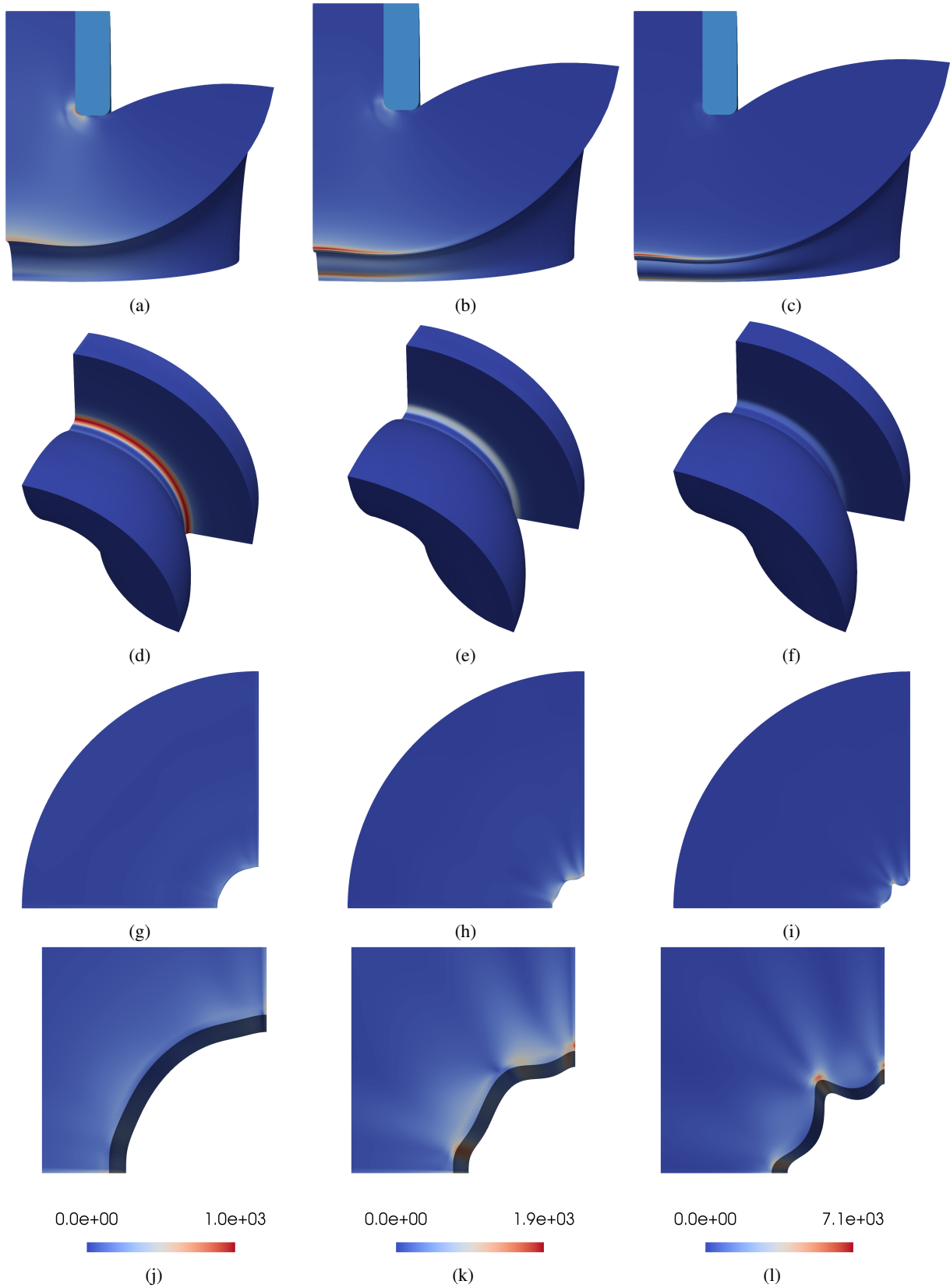


Figure 21: Example 3: Von Mises equivalent stress at steps 360, 400, and 425 are illustrated in column 1, 2, and 3, respectively. Row 1: +x-plane view, Row 2: 3D view, Row 3: +z-plane view, and , Row 4: +z-plane view detailed view at the center (c.f. Figures 19a and 19b).

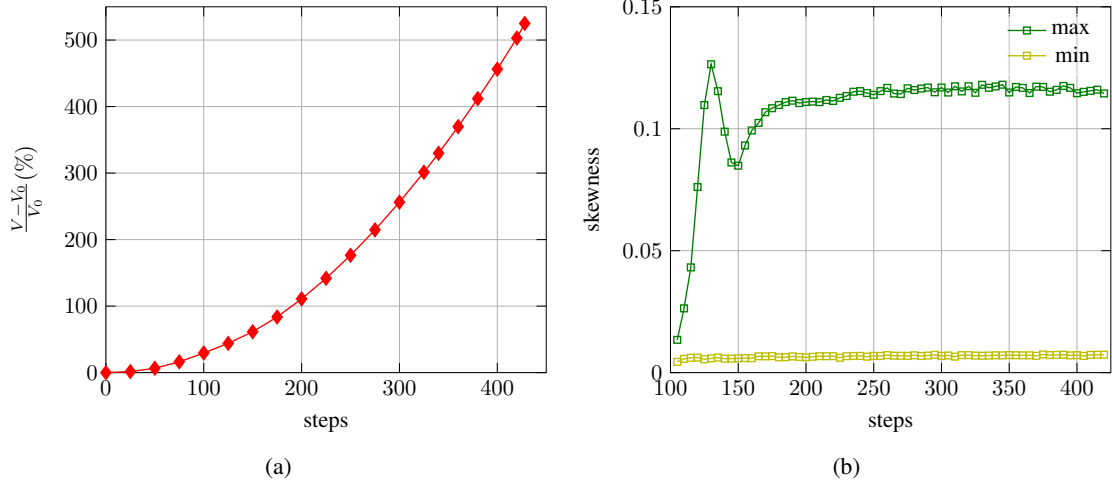


Figure 22: Example 3: (a) percentage change in volume over time. (b) minimum and maximum skewness near the corner.

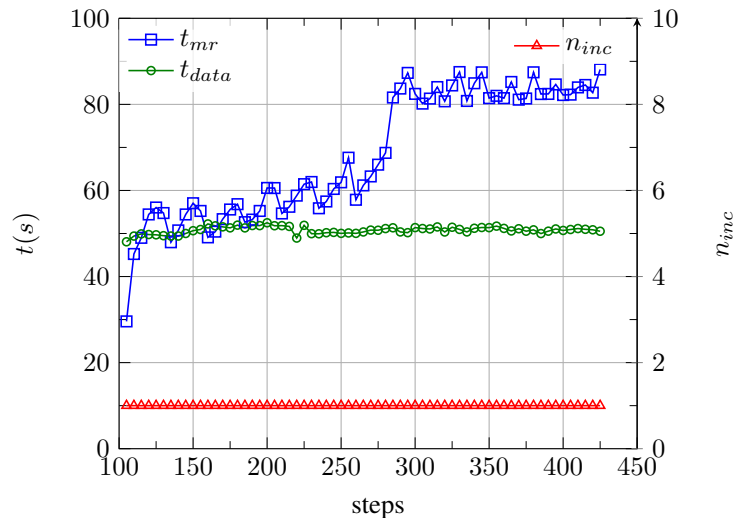


Figure 23: Example 3: Computation time viz, time for mesh refitting step t_{mr} per incrementation steps n_{inc} and data mapping t_{data} time for each mesh adaptation step.

using the iterative GMRES method with AMG(BGS) preconditioner. The convergence tolerance on the combined residual and the increment is set to 10^{-8} . The thermo-mechanical problem is analyzed for 500 steps with time step size $\Delta t = 0.05$.

The mesh adaptation problem is formulated as follows: To achieve a good quality mesh around the corner edge $\mathcal{C}_{r=r_{oi}}$ (see Figure 19), we employ a mesh localization as in (46) with reference length as in (45). The function $f(\mathbf{X})$ as shown in (47) is reformulated as

$$f(\mathbf{X}) = \exp(-c(r_n^2 + r_{ei}^2 - 2r_n r_{ei} + (z - l_e)^2)), \tag{54}$$

with $r_n = x^2 + y^2$ and $c = 150$. The mesh refitting parameters are the same as in the previous example (see Table 2). The mesh sliding surfaces are denoted by $\Gamma_m^{(1),1}$ and $\Gamma_m^{(1),2}$ in Figure 19. Furthermore, a Dirichlet boundary condition is applied to the nodes on the curve $\mathcal{C}_{r=r_{oi}}$ to minimize any potential topology change. The convergence tolerance for the residual and displacement increment is chosen to 10^{-5} . In contrast to previous examples, the linearized system is solved iteratively using the GMRES method with an AMG preconditioner. The data transfer of the scalar is done using the moving least square with trilinear shape function and the tensors using the technique 'R-MLS' with trilinear basis. The mesh adaptation is carried out every 5th step starting from step 100. Finally, the computation is carried out on 9 nodes (216 CPUs) of an Intel Xeon E5-2680v3 2.5GHz processor.

The deformed states at time steps 360, 400, and 428 are depicted in Figures 20.A and 20.B. In step 428, instabilities are observed in the system, and the simulation can no longer be continued. At this step, the expanded material almost closes the annular opening with a minimum inner radius of approximately 0.3545 ($= 0.118 r_{ei}$). The Von Mises equivalent stress at steps 360, 400, and 425 are depicted in Figure 21. Like the previous example, the equivalent stress is initially higher near the fillet $C_{r=r_{oi}}$ (see Figures 21a, 21d, 21g and 21j). But when instabilities started forming the position of the peak equivalent stress shifts to these locations as portrayed in Figures 21b, 21c, 21e, 21f, 21h, 21i, 21k and 21l.

The volume increase during expansion is showcased in Figure 22a with a final volume increase of 525%. Again similar to the previous examples, the quality of mesh around the rigid body (Figures 20.Bg to 20.Bi) is preserved. The minimum and maximum skewness change around the curved edge $C_{r=r_{oi}}$ over time is depicted in Figure 22b. Here only the elements satisfying the condition $0.8 < f(\mathbf{X}_e) < 1.0$ where $f(\mathbf{X}_e)$ is given by (54) with $c = 1$ and \mathbf{X}_e is the element centroid are considered. It can be seen that the skewness is < 0.15 during the expansion process.

Finally, the computational costs are shown in Figure 23. The mesh adaptation problem is solved in a single step, i.e., $n_{inc} = 1$. Here the data is transferred in approximately 50s, and the average t_{mr} is around 70s. However, the average time spent is 119s. The total simulation time is approximately 27h wherein the mesh adaptation accounts for a share of $\approx 5\%$.

5 Conclusion

In the present work, a novel mesh regularization method has been proposed. The mesh regularization scheme relies on an element distortion potential derived from the skewness and aspect ratio of the element. The regularized mesh is found by minimizing this potential. Furthermore, by the definition of spatial functions mesh localization is achieved, which is required for problems with highly localized mesh distortion. To obtain quality meshes at the boundary, we employed a mesh-sliding algorithm based on variationally consistent mortar methods, which enables unrestricted tangential motion of nodes. To transfer the history data, such as tensor-valued data, from the old mesh to the new mesh a structure-preserving invariant interpolation scheme for second-order tensors, which has been proposed in our previous work, is used. These methods fulfill the fundamental requirements of continuum mechanics, such as objectivity and positive definiteness.

The investigations illustrate that the proposed method is well-suited for multi-physics problems such as thermo-mechanical contact problems. Moreover, the studies show that the proposed method produces good-quality mesh for problems involving significant surface deformation (e.g., frictional contact, elasto-plastic contact). The mesh adaptation scheme can restore good-quality meshes for a pure tangential deformation with the help of mesh sliding. Furthermore, for a very localized surface deformation, it allows to retain the initial refined mesh or refine it further using spatial functions for mesh localization. The numerical investigation of very large expansion revealed that the proposed mesh adaptation scheme is well-suited for resolving localized mesh distortion with reasonable computational costs. It is demonstrated that a small element skewness is maintained at the critical regions during such a large expansion. The computational time for mesh adaptation can be kept reasonably low for very large problems with the use of standard iterative solvers with suitable preconditioners as mesh adaptation problem is well-natured. The simulations including mesh adaptation are way more robust and thereby enabling the investigations of scenarios that would not have been accessible without mesh adaptation.

Acknowledgments

The authors acknowledge the financial support from the European Union’s Horizon 2020 research and innovation program under the Marie Skłodowska-Curie grant agreement No 764636.

References

- [1] MM Selim and RP Koomullil. Mesh Deformation Approaches—A Survey. *Journal of Physical Mathematics*, 7(2):1–9, 2016.
- [2] Joe F Thompson, Zahir UA Warsi, and C Wayne Mastin. *Numerical Grid Generation: Foundations and Applications*. Elsevier North-Holland, Inc., 1985.
- [3] Yong Zhao and Ahmed Forhad. A general method for simulation of fluid flows with moving and compliant boundaries on unstructured grids. *Computer Methods in Applied Mechanics and Engineering*, 192(39-40):4439–4466, 2003.

- [4] Aukje De Boer, Martijn S Van der Schoot, and Hester Bijl. Mesh deformation based on radial basis function interpolation. *Computers & Structures*, 85(11-14):784–795, 2007.
- [5] John T Batina. Unsteady Euler Airfoil Solutions Using Unstructured Dynamic Meshes. *AIAA Journal*, 28(8):1381–1388, 1990.
- [6] Charbel Farhat, Christoph Degand, Bruno Koobus, and Michel Lesoinne. Torsional springs for two-dimensional dynamic unstructured fluid meshes. *Computer Methods in Applied Mechanics and Engineering*, 163(1-4):231–245, 1998.
- [7] Frederic J Blom. Considerations on the spring analogy. *International Journal for Numerical Methods in Fluids*, 32(6):647–668, 2000.
- [8] Carlo L Bottasso, Davide Detomi, and Roberto Serra. The ball-vertex method: a new simple spring analogy method for unstructured dynamic meshes. *Computer Methods in Applied Mechanics and Engineering*, 194(39-41):4244–4264, 2005.
- [9] P.I. Crumpton and M.B. Giles. Implicit time–accurate solutions on unstructured dynamic grids. *International Journal for Numerical Methods in Fluids*, 25(11):1285–1300, 1997.
- [10] Clarence Burg. Analytic study of 2D and 3D grid motion using modified Laplacian. *International Journal for Numerical Methods in Fluids*, 52(2):163–197, 2006.
- [11] Andrew A Johnson and Tayfun E Tezduyar. Mesh update strategies in parallel finite element computations of flow problems with moving boundaries and interfaces. *Computer Methods in Applied Mechanics and Engineering*, 119(1-2):73–94, 1994.
- [12] Wolfgang A Wall. *Fluid-Struktur-Interaktion mit stabilisierten Finiten Elementen*. PhD thesis, Universität Stuttgart, 1999.
- [13] Lori A Freitag and Patrick Knupp. Tetrahedral Element Shape Optimization via the Jacobian Determinant and Condition Number. Technical report, Sandia National Lab.(SNL-NM), Albuquerque, NM (United States), 1999.
- [14] Patrick Knupp. Matrix Norms & the Condition Number: A general framework to improve mesh quality via node-movement. Technical report, Sandia National Lab.(SNL-NM), Albuquerque, NM (United States), 1999.
- [15] Zhi Yang and Dimitri J. Mavriplis. Mesh Deformation Strategy Optimized by the Adjoint Method on Unstructured Meshes. *AIAA Journal*, 45(12):2885–2896, 2007.
- [16] Olgierd C Zienkiewicz and Jian Z Zhu. A simple error estimator and adaptive procedure for practical engineering analysis. *International Journal for Numerical Methods in Engineering*, 24(2):337–357, 1987.
- [17] Olgierd Cecil Zienkiewicz and Jian Zhong Zhu. The superconvergent patch recovery and a posteriori error estimates. Part 1: The recovery technique. *International Journal for Numerical Methods in Engineering*, 33(7):1331–1364, 1992.
- [18] Olgierd Cecil Zienkiewicz and Jian Zhong Zhu. The superconvergent patch recovery and a posteriori error estimates. Part 2: Error estimates and adaptivity. *International Journal for Numerical Methods in Engineering*, 33(7):1365–1382, 1992.
- [19] H. Gu, Z. Zong, and K.C. Hung. A modified superconvergent patch recovery method and its application to large deformation problems. *Finite Elements in Analysis and Design*, 40(5-6):665–687, 2004.
- [20] Delphine Brancherie, Pierre Villon, and Adnan Ibrahimbegovic. On a consistent field transfer in non linear inelastic analysis and ultimate load computation. *Computational Mechanics*, 42(2):213–226, 2008.
- [21] Temesgen M. Kindo, Tod A. Laursen, and John E. Dolbow. Toward robust and accurate contact solvers for large deformation applications: a remapping/adaptivity framework for mortar-based methods. *Computational Mechanics*, 54(1):53–70, 2014.
- [22] Abhiroop Satheesh, Christoph P. Schmidt, Wolfgang A. Wall, and Christoph Meier. Structure-Preserving Invariant Interpolation Schemes for Invertible Second-Order Tensors. *Submitted for publication, arXiv preprint arXiv:2211.16507*, 2023.
- [23] E.H. Lee and D.T. Liu. Finite-Strain Elastic-Plastic Theory with Application to Plane-Wave Analysis. *Journal of Applied Physics*, 38(1):19–27, 1967.
- [24] Edward K. Rodriguez, Anne Hoger, and Andrew D. McCulloch. Stress-dependent finite growth in soft elastic tissues. *Journal of Biomechanics*, 27(4):455–467, 1994.
- [25] V.A. Lubarda and A. Hoger. On the mechanics of solids with a growing mass. *International Journal of Solids and Structures*, 39(18):4627–4664, 2002.

- [26] Gerhard A. Holzapfel. *Nonlinear Solid Mechanics: A Continuum Approach for Engineering Science*. *Meccanica*, 37(4):489–490, 2002.
- [27] Barbara I. Wohlmuth. A Mortar Finite Element Method Using Dual Spaces for the Lagrange Multiplier. *SIAM Journal on Numerical Analysis*, 38(3):989–1012, 2000.
- [28] Barbara I. Wohlmuth. Iterative Solvers Based on Domain Decomposition. In *Discretization Methods and Iterative Solvers Based on Domain Decomposition*, pages 85–176. Springer, 2001.
- [29] A. Popp, M. Gitterle, M. Gee, and W.A. Wall. A dual mortar approach for 3d finite deformation contact with consistent linearization. *International Journal for Numerical Methods in Engineering*, 83(11):1428–1465, 2010.
- [30] S. Hübner and B.I. Wohlmuth. Thermo-mechanical contact problems on non-matching meshes. *Computer Methods in Applied Mechanics and Engineering*, 198(15-16):1338–1350, 2009.
- [31] Alexander Seitz, Wolfgang A. Wall, and Alexander Popp. A computational approach for thermo-elasto-plastic frictional contact based on a monolithic formulation using non-smooth nonlinear complementarity functions. *Advanced Modeling and Simulation in Engineering Sciences*, 5(1):1–37, 2018.
- [32] M. Dittmann, M. Franke, İ Temizer, and C. Hesch. Isogeometric Analysis and thermomechanical Mortar contact problems. *Computer Methods in Applied Mechanics and Engineering*, 274:192–212, 2014.
- [33] Daniel Pantuso, Klaus-Jürgen Bathe, and Pavel A. Bouzinov. A finite element procedure for the analysis of thermo-mechanical solids in contact. *Computers & Structures*, 75(6):551–573, 2000.
- [34] Markus Gitterle. *A dual mortar formulation for finite deformation frictional contact problems including wear and thermal coupling*. Dissertation, Technische Universität München, München, 2012.
- [35] Alexander Seitz, Wolfgang A. Wall, and Alexander Popp. Nitsche’s method for finite deformation thermomechanical contact problems. *Computational Mechanics*, 63(6):1091–1110, 2019.
- [36] Alexander Seitz. *Computational Methods for Thermo-Elasto-Plastic Contact*. PhD thesis, Technische Universität München, München, 2019.
- [37] Tod A. Laursen. *Computational Contact and Impact Mechanics: Fundamentals of Modeling Interfacial Phenomena in Nonlinear Finite Element Analysis*. Springer Science & Business Media, 2003.
- [38] Michael A. Puso and Tod A. Laursen. A mortar segment-to-segment contact method for large deformation solid mechanics. *Computer Methods in Applied Mechanics and Engineering*, 193(6-8):601–629, 2004.
- [39] Caroline Danowski, Volker Gravemeier, Lena Yoshihara, and Wolfgang A. Wall. A monolithic computational approach to thermo-structure interaction. *International Journal for Numerical Methods in Engineering*, 95(13):1053–1078, 2013.
- [40] Francisc Verdugo and Wolfgang A. Wall. Unified computational framework for the efficient solution of n -field coupled problems with monolithic schemes. *Computer Methods in Applied Mechanics and Engineering*, 310:335–366, 2016.
- [41] BACI. A Comprehensive Multi-Physics Simulation Framework, accessed: August 09, 2022. URL <https://baci.pages.gitlab.lrz.de/website/>.
- [42] J.C. Simo and C. Miehe. Associative coupled thermoplasticity at finite strains: Formulation, numerical analysis and implementation. *Computer Methods in Applied Mechanics and Engineering*, 98(1):41–104, 1992.
- [43] Christoph Meier, Alexander Popp, and Wolfgang A Wall. Geometrically exact finite element formulations for slender beams: Kirchhoff–Love theory versus Simo–Reissner theory. *Archives of Computational Methods in Engineering*, 26(1):163–243, 2019.
- [44] A. Prakash, W.G. Nöhring, R.A. Lebensohn, H.W. Höppel, and E. Bitzek. A Multiscale Simulation Framework of the Accumulative Roll Rounding Process Accounting for Texture Evolution. *Materials Science and Engineering: A*, 631:104–119, 2015.
- [45] Karol Frydrych, Katarzyna Kowalczyk-Gajewska, and Aruna Prakash. On solution mapping and remeshing in crystal plasticity finite element simulations: application to equal channel angular pressing. *Modelling and Simulation in Materials Science and Engineering*, 27(7):075001, 2019.
- [46] M. Dittmann, F. Aldakheel, J. Schulte, F. Schmidt, M. Krüger, P. Wriggers, and C. Hesch. Phase-field modeling of porous-ductile fracture in non-linear thermo-elasto-plastic solids. *Computer Methods in Applied Mechanics and Engineering*, 361:112730, 2020.
- [47] Sebastian D. Proell, Wolfgang A. Wall, and Christoph Meier. A simple yet consistent constitutive law and mortar-based layer coupling schemes for thermomechanical macroscale simulations of metal additive manufacturing processes. *Advanced Modeling and Simulation in Engineering Sciences*, 8(1):1–37, 2021.

- [48] Sebastian D. Proell, Wolfgang A. Wall, and Christoph Meier. On phase change and latent heat models in metal additive manufacturing process simulation. *Advanced Modeling and Simulation in Engineering Sciences*, 7(1):1–32, 2020.
- [49] Sebastian D. Proell, Peter Munch, Wolfgang A. Wall, and Christoph Meier. A highly efficient computational framework for fast scan-resolved simulations of metal additive manufacturing processes on the scale of real parts. *Submitted for publication, arXiv preprint arXiv:2302.05164*, 2023.